Universiteit Utrecht

Faculty of Science

On the structure and optical properties of quasicrystals

Master Thesis

Bas Doorenbos

Theoretical Physics & Mathematical Sciences

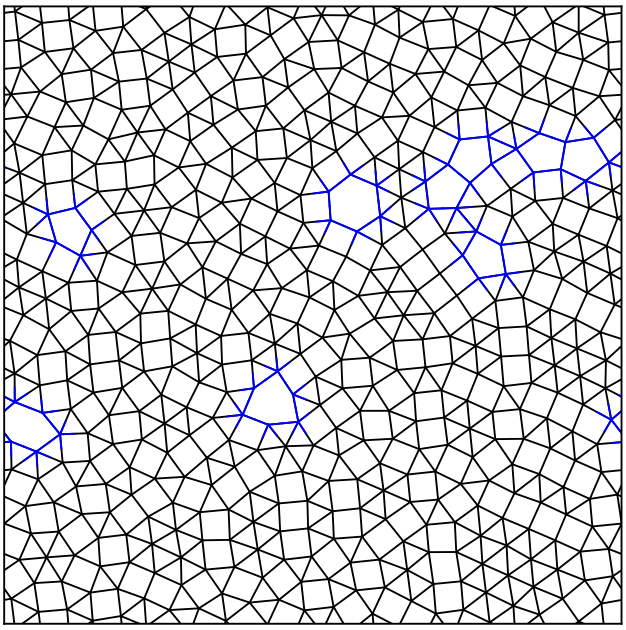

Supervisors:

L. Filion
Debye Institute for Nanomaterials Science, Utrecht University

J. de Graaf
Institute for Theoretical Physics, Utrecht University

M. Schlottbom
Mathematics of Computational Science, Twente University

R. Bisseling
Mathematisch Instituut, Utrecht University

July 2021

Abstract

Quasicrystals are aperiodic structures with long range orientational order. They often posses higher rotational symmetries than is allowed for crystals. Quasicrystals have been both created in a lab and found in nature. Colloidal systems also have been observed to self assemble into quasicrystals. As colloidal systems can be created with length scales that interact with visible light, colloidal quasicrystals have been proposed as materials which might have interesting photonic properties. In this thesis, we make some first steps to addressing how colloidal quasicrystals interact with light. We do this by exploring the structure and defects of a quasicrystal and examining how we can adapt a finite element method, which can be used to solve Maxwell's equations, to the structure of quasicrystals. With respect to the structure of quasicrystals, we use a Monte Carlo method in order to study the self assembly of two-dimensional core corona particles into a quasicrystal. We study the formation of defects through the colloidal quasicrystals and develop a method in order to identify defects in the quasicrystal. Using this method we follow defects moving through the quasicrystal and calculate the diffusion coefficient for different temperatures and packing fractions. With respect to the optical properties of quasicrystals, we propose a finite element method that is adapted to the structure of a one dimensional photonic quasicrystal. We apply this method to a simplification of Maxwell's equations and study the convergence of this method.

Contents

1 Introduction

1.1 Colloids

Colloids are small particles suspended in a solvent. They come in a wide variety of shapes. Particles are usually considered to be colloids if they have a diameter of 1 nm to 1 µm [1, 2]. Examples of colloidal systems include aerosols, foams, ink and plastics [2]. A Scottish botanist, named Robert Brown, first observed that colloids perform random motion, when he studied pollen grains of the plant Clarkia pulchella [3]. This random motion of colloids in their solvent was later named *Brownian motion*. At first it was thought that the motion was because of life related processes [3]. However, this explanation was ruled out after lifeless colloids were observed to exhibit Brownian motion as well. A more satisfying explanation for Brownian motion was given by Albert Einstein in 1905 [4]. Brownian motion is explained by the interaction between colloidal particles and particles in the solvent. This Brownian motion allows the particles to move and even assemble into a wide variety of structures. This process of particles ordering themselves into a structure is called *self-assembly*. Colloids have been used as models for atomic and molecular systems, because they exhibit many of the phases of these systems [5]. Because of their size, colloidal particles can be followed using confocal microscopes [5]. This allows for studying self-assembly of colloidal systems in real time. Additionally, colloids undergo phase transitions and therefore can be used to study phase transitions. A simple example can be found in hard spheres, which you can think of as billiard balls at colloidal size. It has been shown that a system of hard spheres of equal size undergoes a phase transition from a fluid to a crystal phase [6]. However, since a hard sphere system has no finite energy difference between states, its equilibrium phase only depends on the packing fraction. Adding a soft layer to the particles unlocks a rich variety of behaviour depending on the properties of this soft layer. In this thesis, we study particles with a soft corona layer. It has been shown that a system of such particles exhibits a wide variety of equilibrium phases, one of which is the quasicrystal phase [7].

1.2 Quasicrystals

A quasicrystal is a structure that has long range order, but no periodicity. Quasicrystals have been discovered only quite recently. In the late 1970s Paul Steinhardt had imagined that crystals with five-fold symmetry might be possible [8]. In 1982, materials scientist Dan Shechtman found a diffraction pattern with five-fold symmetry, for a rapidly cooled alloy of aluminium and manganese. He had discovered the first quasicrystal! He published his findings in 1984 [9]. After publishing these observations, Shechtman was met with pushback. The head of his laboratory suggested he read a book on X-ray diffraction. At one conference, Nobel prize laureate Linus Pauling exclaimed: “Danny Shechtman is talking nonsense, there are no quasi-crystals, just quasi-scientists” [10]. Eventually however, Shechtman was vindicated and won the Nobel prize for Chemistry in 2011 [11]. The quasicrystal that Shechtman discovered was made in a lab. Steinhardt was inspired by Shechtman’s discovery and set out on an expedition to find naturally occuring quasicrystals. On 2 January 2009, he, together with other researchers, became certain that they found a natural quasicrystal, which probably originated from a meteor [8].
One of the first applications of a quasicrystal was as a coating for non-stick frying pan [12]. This coating had a similar function to Teflon, but does not wear out. However, the production of pans coated with quasicrystals has stopped, because too much salt would etch the coating [13].
Another use of quasicrystals is in steel. A Swedish company, named Sandvik, produces steel which is strengthened by small quasicrystalline particles [13]. This steel is used in e.g. razor blades and surgery tools. In this thesis, we will be exploring another application: quasicrystals for photonic materials.

1.3 Photonic crystals

A photonic crystal is a periodic structure of materials with different refractive indices. Such a structure interacts with light in peculiar ways. Depending on the exact structure, frequencies may exist which are unable to pass through the photonic crystal and which are thus reflected. A range of frequencies for which light cannot pass through a photonic crystal is called a *band gap* [14]. Photonic band gaps are what gives some butterfly wings their colors [15]. The structure of a periodic crystal is similar to a conventional crystal

in the sense that in principle, the entire structure consists of a repeated unit cell. An important difference is the scale of the lattice constant, which indicates the scale of periodicity. For most atomic crystals, this lattice constant is on the order of ångströms, while for photonic crystals, the lattice constant must be on the order of the wavelength of the relevant electromagnetic waves [14]. The visible spectrum consists of electromagnetic waves with wave lengths between 380 and 740 nm. This is commensurate with the size of colloidal particles. This means that colloidal crystals are suitable candidates for photonic crystals [16].
Similar to photonic crystals are photonic quasicrystals. Photonic quasicrystals have similar structure to most atomic quasicrystals, but have a similar characteristic length to photonic crystals. Similar to photonic crystals, photonic quasicrystals can also have bandgaps [17]. Furthermore anisotropy of the band gap is dependent on the symmetry of the underlying structure of the photonic material. Photonic quasicrystals can possess a higher rotational symmetry than photonic crystals, which means it might be easier to construct a photonic quasicrystal with a bandgap with the same frequency in all directions [18]. This is referred to as a complete band gap.

1.4 Aim of this thesis

The aim of this thesis is to study photonic properties of colloidal quasicrystals. In order to do this, we need to study the structure of a quasicrystal and then solve Maxwell's equations on this underlying structure. We will study a system of colloidal core corona particles. These particles have been observed to form quasicrystals [7]. We will verify that this is true by letting a such a system self-assemble into a quasicrystal. We will study possible defects in this self-assembled system. Furthermore, we will take a closer look at defects in isolation. In order to study the photonic properties of a quasicrystal, we need to solve Maxwell's equations on the quasicrystal. We make a first step of creating a finite elements method, which is adapted to the structure of a quasicrystal. Furthermore, we study the convergence of this method.

2 Theory

2.1 Crystals versus quasicrystals

One of the most common phases of matter is a crystal. The particles that make up a crystal range from ions, such as table salt, and simple molecules, such as ice, to more complex molecules such as insulin [19]. On a larger scale, colloids can also form crystals. A crystal is characterized by periodically repeating arrangements of particles. The smallest unit of these particles, which is large enough to carry the structure of the crystal is called the *unit cell*. Unit cells come in different shapes, e.g. a square or hexagon (see Figure 2.1).
Interestingly, it has been shown that for periodic structures, there are only certain allowed rotational symmetries, due to the crystallographic restriction theorem. These are 2, 3, 4 and 6-fold symmetries.
One of the classic ways to recognize a crystal is via its diffraction pattern. This diffraction pattern shows the same rotational symmetry as the crystal itself. This means that the diffraction pattern of a crystal can only have 2, 3, 4 or 6-fold symmetries, like the crystal itself. However, this begs the question: do structures exist which show other rotational symmetries in their diffraction patterns? In Ref. [9], Shechtman shows that such structures indeed exist. Figure 2.2 shows an electron diffraction pattern of an alloy of aluminum with manganese. This diffraction pattern shows a fivefold symmetry. The sharp diffraction peaks indicate a high long-range orientational order. Since the diffraction pattern shows a symmetry which is forbidden for periodic crystals, this must be an aperiodic structure.
Whereas a crystal is built up by one periodically repeating unit cell, a quasicrystal can be built up by a number of different subpatterns, although quasicrystals are sometimes described by quasi unit cells [20]. In two dimensions, filling space using these subpatterns, or tiling cells, is called a tiling. An ordinary crystal is built out of a periodically repeating unit cell. This means that the crystal corresponds to a periodic tiling of this unit cell. Two examples of such tilings are given in Figures 2.3a and 2.3b. Quasicrystals, on the other hand, can be built from multiple tiling cells. These multiple tiling cells create an aperiodic tiling, e.g. Figure 2.3c. Such tilings have high orientational ordering, similar to crystals. However, these aperiodic tilings are allowed higher rotational symmetries, e.g. ten-fold or twelve-fold, than periodic tilings.

2.2 Colloidal model system

Quasicrystalline behaviour usually arises from the presence of two competing length scales [21], although competing length scales are not a necessity [22]. There are at least two ways of introducing two length scales in a colloidal system. One is to have a two component system, e.g. a system of two types of hard spheres with different diameters. Two length scales can also be introduced in a single component system where two competing length scales are introduced by the interaction potential between the particles. In this thesis such a single-component system is studied. We study a single component system of particles with a hard core and a soft corona.

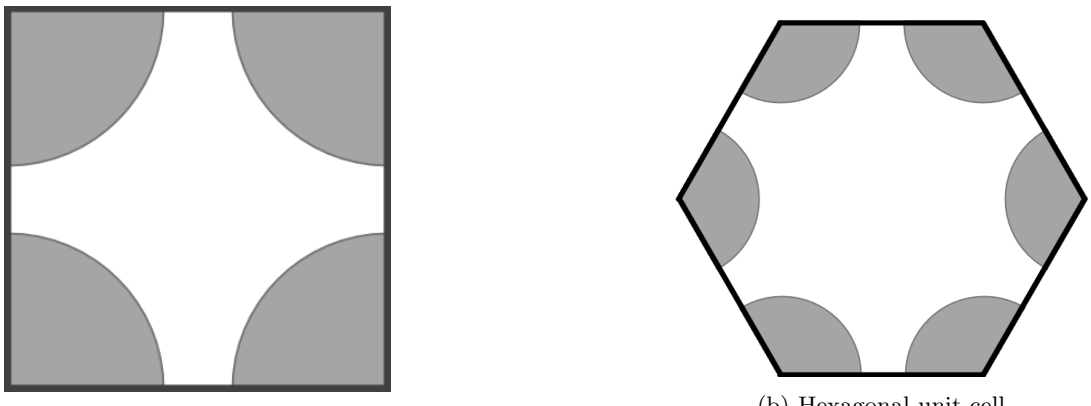

(a) Square unit cell

(b) Hexagonal unit cell

Figure 2.1: Examples of unit cells of crystals.

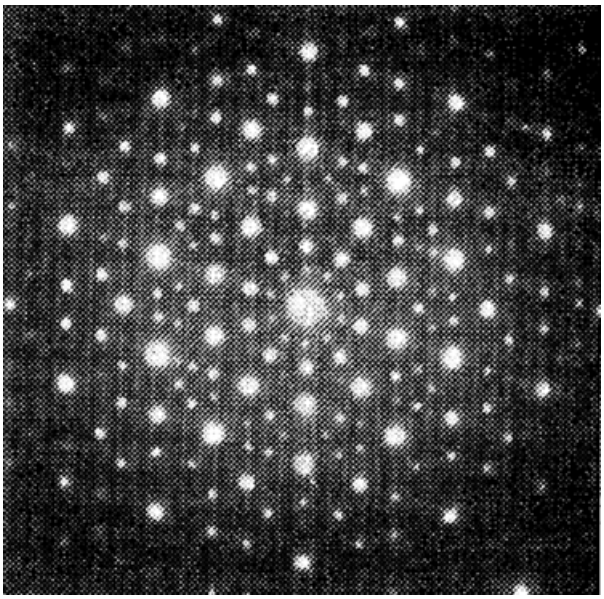

Figure 2.2: Electron diffraction pattern of rapidly cooled alloys of Al with 14 at.% Mn. Reprinted from [9].

2.3 Core corona particle

The particles studied in this thesis are interact via a rotationally symmetric hard-core square shoulder (HCSS) pair potential. The potential of a core corona particle is given by

$$V_{\mathrm{HCCS}}(r) = \begin{cases} \infty & r < \sigma_{\mathrm{HD}}, \\ \varepsilon & \sigma_{\mathrm{HD}} < r < \delta, \\ 0 & \delta < r, \end{cases} \tag{2.1}$$

where r is the center of mass distance between two particles, ϵ is the height of the square shoulder, δ is the width of the square shoulder and σ_{HD} is the diameter of the core. If $\mathbf{r}_i$ is the position of particle i, then the total energy of a system of N core corona particles is simply given by

$$U(\mathbf{r}^N) = \sum_{i=1}^{N} \sum_{j=1}^{i-1} V_{\mathrm{HCCS}}(\mathbf{r}_i - \mathbf{r}_j). \tag{2.2}$$

The phase behaviour is influenced not only by the density of the system, but also by the shoulder width δ. At $\delta \sim \sigma_{\mathrm{HD}}$, the particles behave similar to hard spheres. On the other hand, for $\delta \gg \sigma_{\mathrm{HD}}$ at low temperatures, the hard core becomes effectively irrelevant. A phase diagram for $\delta = 1.4\sigma_{\mathrm{HD}}$ is shown in Figure 2.5. Here $\rho^* = N\sigma_{\mathrm{HD}}^2/V$ is the reduced density and $T^* = k_B T/\varepsilon$ is the reduced temperature. In this thesis, we will mostly discuss density in terms of the packing fraction η, which is defined as $\eta = \pi N \sigma_{\mathrm{HD}}^2/4V$. The phase diagram shows a rich variety of equilibrium phase behaviour. Notably, one of the phases is the twelve-fold (dodecagonal) quasicrystal.

2.4 Photonic crystals

A photonic crystal is a periodic structure of dielectric materials. Accordingly, the dielectric coefficient has this same periodicity through the photonic crystal. When an electromagnetic wave propogates through a photonic crystal, the wave interacts with these variations, leading to multiple intriguing effects, such as structural colors, and photonic band gaps [23]. We can understand this behavior using Maxwell's equations as described in this section.

Here, we will assume that the photonic crystal extends infinitely in all directions. Furthermore, we assume that the photonic material is made out of nonmagnetic materials. Let $\mathbf{a}_i$ be the translation vectors such that the position dependent relative permittivity is given by $\varepsilon_r(\mathbf{r}) = \varepsilon_r(\mathbf{r} + \mathbf{a}_i)$, for $i \in \{1, \ldots, N\}$.

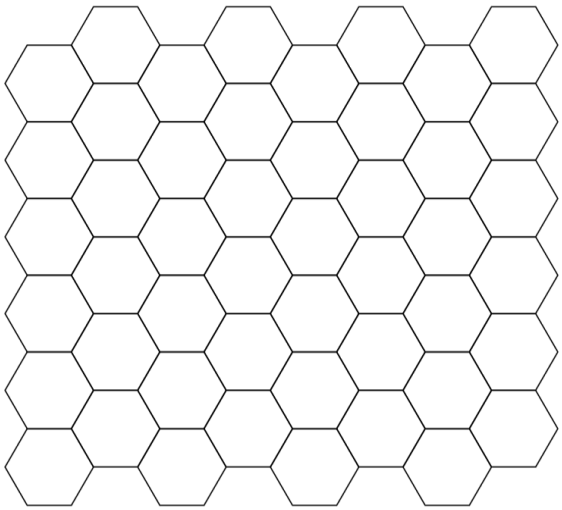

(a) A periodic hexagonal tiling.

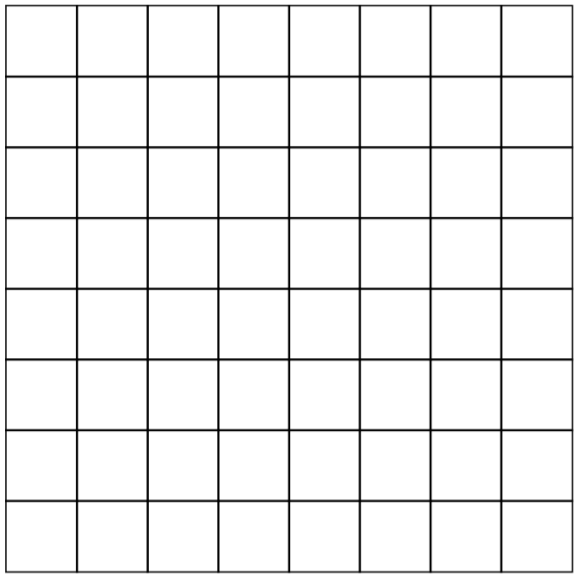

(b) Periodic square tiling

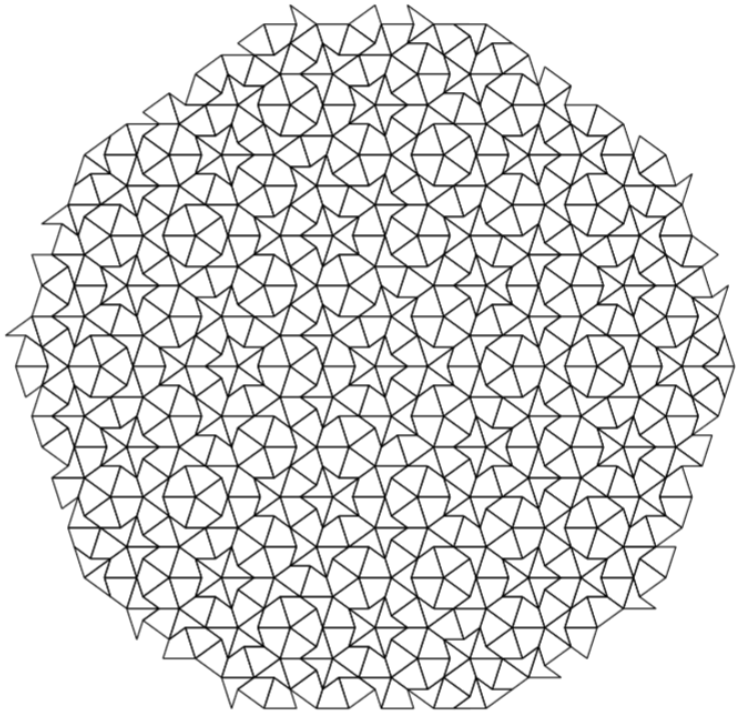

(c) Aperiodic tiling built from two tiling cells.

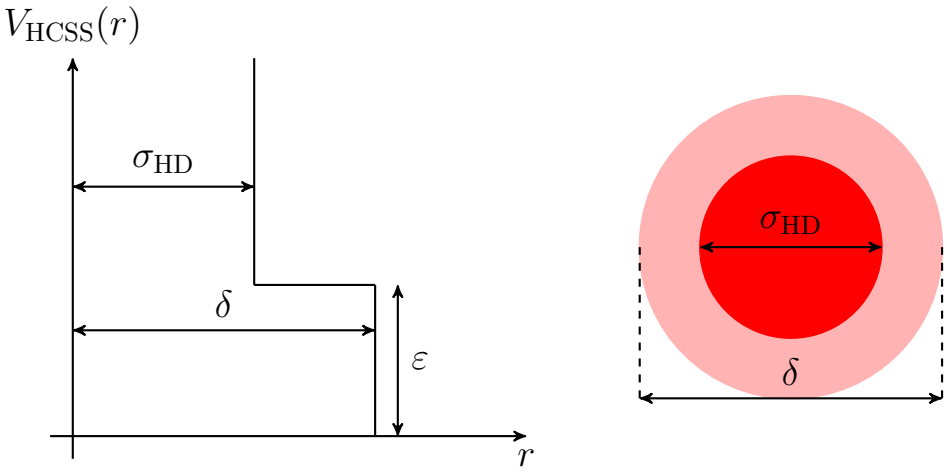

Figure 2.4: Hard-core soft-shoulder (HCSS) potential (left) and visual representation (right) of core-corona particles.

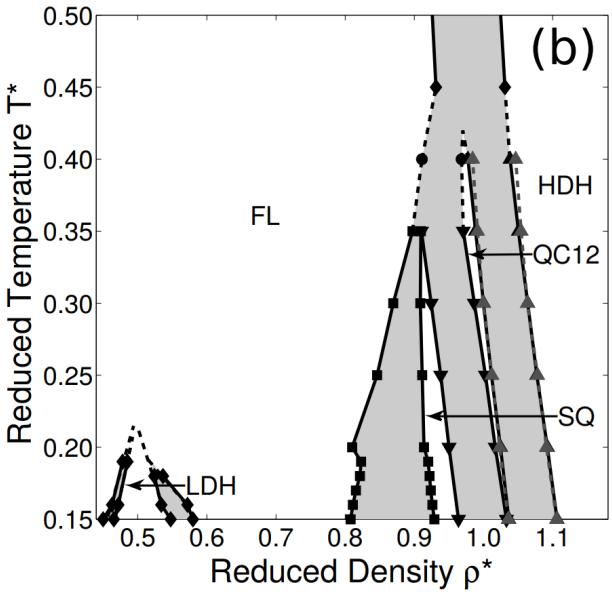

Figure 2.5: Equilibrium phase diagram for a two-dimensional system of hard-core soft-shoulder particles, with shoulder width $\delta = 1.4\sigma_{HD}$. The phases represented are fluid (FL), square (SQ), low-density hexagonal (LDH), high-density hexagonal (HDH), and random-tiling dodecagonal quasicrystal (QC12). The phase boundaries of the QC12 without the entropy correction, that accounts for the number of distinct configurations, are shown with dashed grey lines. Reprinted from Ref. [7].

Now, consider the source free formulations of Faraday's law and Ampére's law, where we assume that the magnetic permeability of the photonic crystal is equal to that in free space:

$$\nabla \times \mathbf{E} = -\mu_0 \frac{\partial \mathbf{H}}{\partial t}, \tag{2.3}$$

$$\nabla \times \mathbf{H} = \varepsilon_0 \varepsilon_r \frac{\partial \mathbf{E}}{\partial t}. \tag{2.4}$$

Here $\mathbf{E}$ is the electric field, $\mathbf{H}$ is the magnetic field, μ_0 is the permeability constant, ε_0 is the electric constant, ε_r is the relative permittivity, and t is time. Dividing (2.4) by ε_r, taking the curl and using (2.3) yields

$$\nabla \times \left(\frac{1}{\varepsilon_r} \nabla \times \mathbf{H} \right) = \nabla \times \left(\varepsilon_0 \frac{\partial \mathbf{E}}{\partial t} \right) = -\mu_0 \varepsilon_0 \frac{\partial^2 \mathbf{H}}{\partial t^2}. \tag{2.5}$$

By using a Fourier transform, we assume that the magnetic field is time-harmonic. We assume that the magnetic field has a temporal frequency $\omega > 0$, such that

$$\frac{\partial \mathbf{H}}{\partial t} = -i\omega \mathbf{H}. \tag{2.6}$$

Plugging this into Equation (2.5) and using that $c^{-1} = \sqrt{\mu_0 \varepsilon_0}$, results in

$$\nabla \times \left(\frac{1}{\varepsilon_r} \nabla \times \mathbf{H} \right) = \left(\frac{\omega}{c} \right)^2 \mathbf{H}. \tag{2.7}$$

For unknown ω, this is an eigenvalue problem. The operator on the left hand side working on $\mathbf{H}$ is Hermitian, which means that the eigenvalues $\left(\frac{\omega}{c}\right)^2$ are real. Now due to Bloch's theorem, solutions of (2.7) take the form

$$\mathbf{H}(\mathbf{x}) = \mathbf{H}_\mathbf{k}(\mathbf{x}) = \mathbf{u}_\mathbf{k}(\mathbf{x}) e^{i\mathbf{k}\cdot\mathbf{x}}, \tag{2.8}$$

for a wave vector $\mathbf{k}$ and where $\mathbf{u}_\mathbf{k}$ has the same periodicity as ε_r, i.e. $\mathbf{u}_\mathbf{k}(\mathbf{x}) = \mathbf{u}(\mathbf{x} + \mathbf{a}_i)$, for $i \in \{1, \ldots, N\}$. Inserting this into (2.7) yields

$$(\nabla + i\mathbf{k}) \times \left(\frac{1}{\varepsilon_r} (\nabla + i\mathbf{k}) \times \mathbf{u}_\mathbf{k} \right) = \left(\frac{\omega}{c} \right)^2 \mathbf{u}_\mathbf{k}. \tag{2.9}$$

This eigenvalue problem can be solved using numerical methods. The most common method is using a plane wave expansion [24]. One can restrict calculations to only the wave vectors $\mathbf{k}$ along the first the Brillouin zone. Along this Brillouin zone, the dispersion relation can be calculated. These dispersion relations form a photonic band diagram. If for a certain frequency ω there exists no corresponding wave vector, then $(\omega/c)^2$ is not an eigenvalue for (2.9). Hence, for frequency ω there exists no valid eigenmmode u_k, which means that light with this frequency is not allowed to pass through the crystal. This is what is called a photonic band gap.

Since a crystal structure has different periodicity in different directions, the photonic band gap is generally also different in different directions. This poses a challenge for creating a photonic crystal with a photonic band gap with the same forbidden frequency in all directions.

Although quasicrystals lack periodicity, they can still have photonic band gaps [18, 25]. Since quasicrystals possess a higher symmetry than crystals, photonic quasicrystals are more favorable for the creation of a photonic band gap with the same frequency in all directions. In Part II, we will explore methods to study the photonic properties of colloidal quasicrystals.

PART I

QUASICRYSTAL STRUCTURE AND DEFECTS

3 Simulation methods

3.1 Monte Carlo method

We use a Monte Carlo method to simulate a single component system of core corona particles at constant number of N particles, 2d-volume (area) V and temperature T, i.e. in the canonical ensemble (NVT). In all cases the system is subject to periodic boundary conditions.
A Monte Carlo simulation in the NVT ensemble allows one to sample configurations according to the Boltzmann distribution. Generating the configurations is done via so-called "trial" moves where we try and make a small change to the state of the system. Note that in order to ensure that the trial moves result in an equilibrium distribution of states, two requirements are necessary: i) that the trial moves obey detailed balance, and ii) ergodicity. Detailed balance means that if a system is in equilibrium, the probability for the system to go from state μ to state ν must be equal to the probability of the system going from state ν to state μ. That is,

$$P_\mu \pi(\mu \to \nu) = P_\nu \pi(\nu \to \mu), \tag{3.1}$$

where P_μ is the probability of the system to be in state μ and $\pi(\mu \to \nu)$ is the transition probability for the system going from μ to ν. Ergodicity demands that the system can reach any state from any other state.
In the case of an NVT system, the standard trial move, which indeed obeys these two requirements, is to try and move a single, random particle by an amount chosen from a uniform distribution. In practice, in each trial move, a randomly selected particle i is displaced by a small amount $d\mathbf{r}$, from $\mathbf{r}^i_{\text{old}}$ to $\mathbf{r}^i_{\text{new}} = \mathbf{r}^i_{\text{old}} + d\mathbf{r}$. This trial move is either accepted or rejected based on the Metropolis acceptance criteria [26]

$$\text{acc}(\mathbf{r}^N_{\text{old}} \to \mathbf{r}^N_{\text{new}}) = \min(1, \exp(-\beta \Delta U)), \tag{3.2}$$

where $\Delta U = U(\mathbf{r}^N_{\text{new}}) - U(\mathbf{r}^N_{\text{old}})$ is the energy difference between the configuration before and after the particle move respectively. If the trial move is rejected, the previous configuration is restored.

3.2 Initialization

In order to simulate the particles in a box, the particles first need to be placed inside this box. This can be done in several ways. One way might be to start from a hexagonal crystal structure. An advantage of this method is that it is easy to implement and will work for any allowed packing fraction. A disadvantage is that the system might get stuck in a meta-stable hexagonal state.
A different way of initializing a starting configuration is putting the particles at random positions in the box at low density, such that the particles do not overlap. From here one can let the particles move according to Monte Carlo steps and after a certain number of steps try to scale down the box and scaling the particles positions with it, in order to increase the density. Algorithm 1 shows how this can be done. However, it may take a long time for this algorithm to get up to the desired density. In order to speed up the initialization, an extra repulsive potential can be added, see e.g. Figure 3.1. This extra potential pushes particles away from each other. This prevents overlapping particles after down scaling of the volume. The goal of this potential is to create gaps between particles such that they can be pushed closer together. A good candidate for such a potential is

$$\beta V(\mathbf{r}) = \begin{cases} \infty & |\mathbf{r}| \le \sigma_{\text{HD}}, \\ \frac{\bar{\sigma}^2 - |\mathbf{r}|^2}{|\mathbf{r}|^2 - \sigma^2_{\text{HD}}} & \sigma_{\text{HD}} \le |\mathbf{r}| \le \bar{\sigma}, \\ 0 & \bar{\sigma} < |\mathbf{r}|, \end{cases} \tag{3.3}$$

for some $\bar{\sigma} > \sigma_{\text{HD}}$.

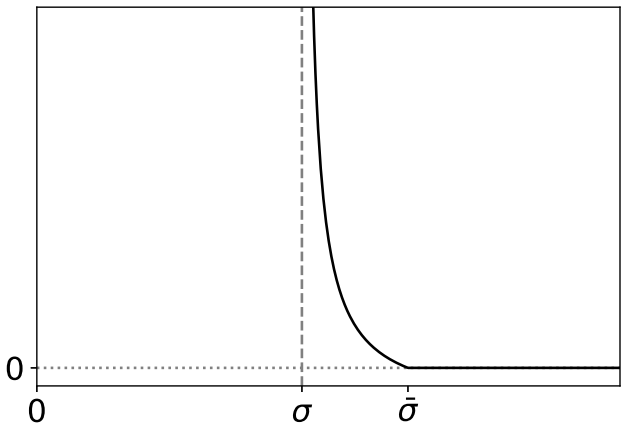

Figure 3.1: Repulsive potential.

Algorithm 1: Initialize configuration.

Result: Random configuration at reduced density ρ^*.
$L_{\text{target}} = \sigma_{\text{HD}}\sqrt{N/\rho^*}$.
$L = 10L_{\text{target}}$.
for $i = 1$ *to* N **do**
  while *no overlap* **do**
    Insert particle i at random position.
  end
end
while $L > L_{target}$ **do**
  for $t = 1$ *to* T **do**
    Move a particle according to Metropolis acceptance criterion.
  end
  `// Scale the box`
  $L = (1 - \epsilon)L$.
  for $i = 1$ *to* N **do**
    $\mathbf{r}_i = (1 - \epsilon)\mathbf{r}_i$.
  end
end
`// If box is scaled down too much, scale up.`
for $i = 1$ *to* N **do**
  $\mathbf{r}_i = (L/L_{\text{target}})\mathbf{r}_i$.
end
$L = L_{\text{target}}$.

One can also initialize the system in a quasicrystalline configuration. In order to do this, one starts by creating a quasicrystalline structure in a small square box of area L^2. This box can be repeated in space for N times in both directions. This creates a larger configuration of particles of area L^2N^2, whose structure locally resembles that of a quasicrystal. However, the box now contains a structure with repeating units of size L^2. In order to get a quasicrystalline structure without repetitions inside the box, we make use of *zipper* moves [27]. These work by introducing two defects in the quasicrystalline lattice. These defects are propagated along a path, along which the underlying tiling is changed, until the defects annihilate. The result is a new quasicrystalline structure. After performing enough of these moves, the repetitiveness of length L is destroyed.

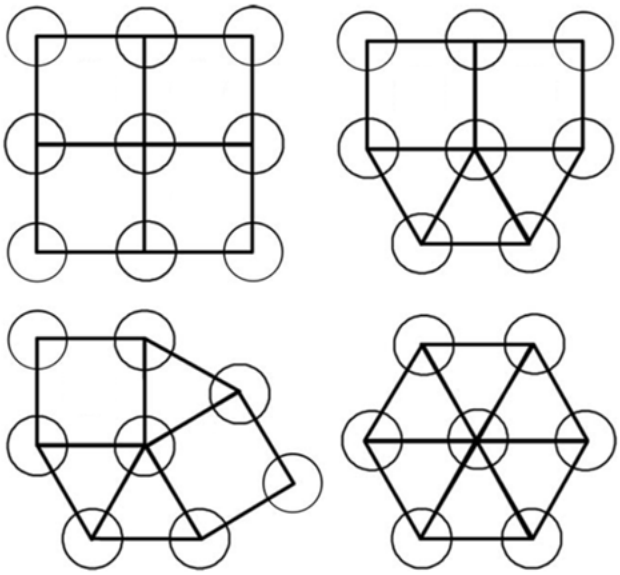

Figure 3.2: All possible configurations in a perfect square-triangle quasicrystal. Altered from [28].

3.3 Locating defects

As we will show in Chapter 4, self-assembled quasicrystals contain a large number of defects. In order to study such defects, a method is needed to locate the defects. In this section, two methods for locating defects are described. The first of these methods is easiest to implement. The second method is less affected by thermal fluctuations, but is harder to implement. Both methods are specific to the dodecagonal quasicrystal, for which the bonds between neighboring particles form a square-triangle tiling of the box. Particles are defined to be neighbors if they are closer than some cutoff radius r_n. Throughout this thesis, we set this cutoff radius at $r_n = 1.27\sigma_{\mathrm{HD}}$.

3.3.1 Method 1

If the bonds between neighboring particles form a square-triangle tiling, then any vertex coinciding with a particle must be part of squares and triangles. There are only three different numbers of squares and triangles that are allowed. A vertex can be part of four squares, two squares and three triangles or six triangles. Up to rotational symmetry there are two different ways to place two squares and three triangles around a vertex. This leaves four possible configurations, which are illustrated in Figure 3.2. If any vertex does not conform to one of these configurations, then we say that the corresponding particle is part of a defect. Then we say that two particles are part of the same defect if they share a bond. This is the first way to classify a defect. This first method is an objective way to classify defects. A drawback of this method is that it is susceptible to thermal fluctuations. If particles are moving around, then neighboring particles could move away from each other enough to break the bond between them, i.e. they separate a distance larger than r_n. This would break the square triangle tiling of the bonds and therefore introduces a defect. However, such a defect does not change the structure and may be resolved in the next step already. This motivates the development of another method to classify defects, which filters out small movements of particles in order to find just the structural defects. Crucial to this method is the idea of uplifting.

3.3.2 Method 2

Consider a square-triangle tiling of the plane. Let the squares and triangles have edges of length d. We introduce the following vectors

$$\mathbf{e}_i = d \begin{pmatrix} \cos(\alpha i) \\ \sin(\alpha i) \end{pmatrix}, \tag{3.4}$$

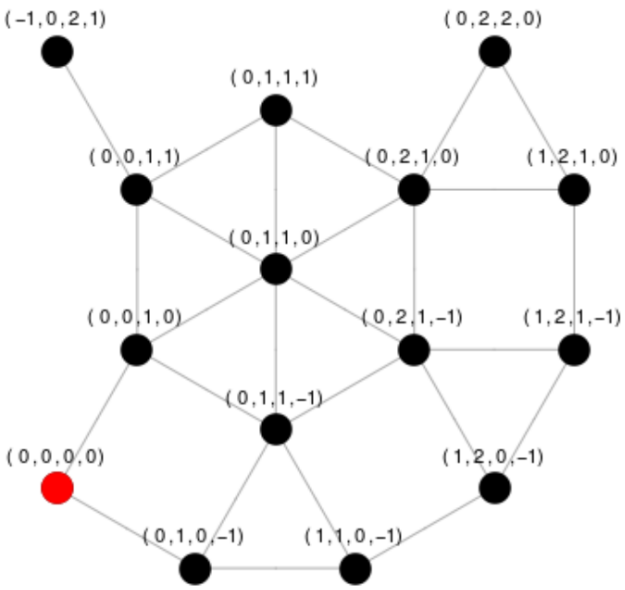

Figure 3.3: Labeling part of a square-triangle tiling. The red point is the origin.

for $i \in \{0, 1, \ldots, 11\}$, with $\alpha = \pi/6$. All edges between vertices lie along one of these vectors. However, we only need four of these vectors to reach any of the vectors in an integer number of steps. After all, $\mathbf{e}_{i+6} = -\mathbf{e}_i$, $\mathbf{e}_4 = \mathbf{e}_2 - \mathbf{e}_0$ and $\mathbf{e}_5 = \mathbf{e}_3 - \mathbf{e}_1$. As a result, $\{\mathbf{e}_0, \mathbf{e}_1, \mathbf{e}_2, \mathbf{e}_3\}$ is a basis for all vertices. Over the field over integers.

We can choose some arbitrary vertex as the origin. Then we can denote the position of any vertex by some 4-vector $\mathbf{q}$ of integers, such that the position is given by $\sum_{i=0}^{3} q_k \mathbf{e}_k$, where q_k are integers. This means that the location of every particle corresponds to a point on a 4-dimensional integer lattice. This is what is meant by uplifting [29]. We take a spatial position of a vertex and 'lift' it to 4D space.

To find the vector $\mathbf{q}$ for the vertices, one designates an arbitrary vertex to be the origin. Then, once the vector $\mathbf{q}$ is known for some vertex, one can assign a $\mathbf{q}$ vector to its neighbors. All neighboring are connected by edges lying along one of the twelve vectors $\mathbf{e}_i$. If the edge to a vertex lies along the direction of $\mathbf{e}_0$, then this corresponds to a change of $(1, 0, 0, 0)$ in the $\mathbf{q}$-space. Starting from the origin vertex, one can iteratively find the 4 vectors for the vertices and lift the entire tiling into 4D space.

Once a tiling is lifted into 4D space, the original spatial positions can be easily recovered. The spatial position $\mathbf{r}_j$ of vertex i with four vector $\mathbf{q}^j$ is given by

$$\mathbf{r}_i = \mathbf{r}_0 + \sum_{i=0}^{3} q_i^j \mathbf{e}_i, \tag{3.5}$$

where we define $\mathbf{r}_0$ as the position of the vertex corresponding to the origin in 4D space.

In this thesis we are working with a finite box subject to periodic boundary conditions. The periodicity in this box also introduces a periodicity in the corresponding 4D space. The $\mathbf{q}$-vectors corresponding to the particles are not uniquely defined. However, this does not pose a problem. The positions in real space are recovered by projecting back to real space and taking the modulo with respect to the box size:

$$\mathbf{r}_i = \mathbf{r}_0 + \sum_{i=0}^{3} q_i^j \mathbf{e}_i \mod \mathbf{b}, \tag{3.6}$$

where $\mathbf{b}$ is the size of the box and the modulo is taken per component. The non-uniqueness of the $\mathbf{q}$-vectors in 4d space is removed by the modulo operation in real space.

The above method of uplifting and projecting back has been described for a perfect square-triangle tiling. We can apply this same method for a thermal quasicrystal, assuming we can assign each bond between

two particles to one of the twelve directions with some certainty. Uplifting and back projection then yields reference positions for the particles in the quasicrystal, where thermal noise is filtered out. One has to be careful with how these bonds are assigned and in what order. Below three different ways of finding the **q**-vectors for all particles are discussed. Each method is a refinement of the previous one. For these methods it is assumed that the bond length d between particles is known.

A naive way is as follows. Choose an initial particle at random and assign to it the 0-vector in **q**-space. From this particle, for each neighbor, choose the direction $\mathbf{e}_j$ that is closest to the bond between the initial particle and the neighbor in question, and assign the corresponding **q**-vector to the neighbor in question. Then take on of the particles for which the **q**-vector has been determined and then determine the **q**-vector of its neighbors, for which the four vector **q** has not been determined yet, in the same way. Continue doing this by taking one particles corresponding to one of the recently added **q**-vectors and determining the **q**-vectors of its neighbors, until all particles have a **q**-vector associated to them. Afterwards shift all particles by a vector ε such that the average distance between the particles and their reference points is zero. This is a relatively simple method of uplifting.

A problem with this method is that if a **q**-vector for a particle is determined along a bond which is formed due to thermal fluctuations, then this particle may be assigned the 'wrong' **q**-vector. Any **q**-vector that is determined based on the **q**-vector of this particle will also be wrong. This means that upon projecting back to the box, an entire region could be formed, where the particles are misplaced. This problem motivates the development of a more thorough method.

For the second method one first uses the method described in Section 3.3 to find defects in the quasicrystal. As stated before, this method will find both structural defects and defects which are due to thermal noise. Now let D be the set of particles classified as a defect by this first method and let P be the set of particles which are at least three neighbors removed from any particle that is part of a defect. Furthermore, let R be the complement of $D \cup P$, i.e. those particles which are themselves not in D, but the first and second neighbors of particles in D. Last of all, let P_b be the set of all bonds between neighboring particles in P. The assignment of **q**-vectors now goes in phases.

1. Choose one particle in P as the initial particle. Then perform the same actions as for the first method to find the **q**-vectors for the particles, but only for particles in P. If P_e forms a connected component, then this method yields a **q**-vector for all particles in P.
2. Now, in the same way, find the **q**-vectors for particles in R.
3. Find the **q**-vectors for particles in D.
4. Shift all particles by a vector ε such that the average displacement between the particles in P and their reference points is the zero vector.

The shift of the center of mass is only calibrated on particles in P, since defects can deform the quasicrystalline lattice.

Since the method as described in Section 3.3 finds all defects which are formed due to an additional bond formation, no **q**-vector will be determined along such a bond when using the method as described above.

One thing that could still be refined is how to assign a bond to one of the twelve allowed directions. For the third method, we change this assignment. One more added change is that for every added **q**-vector it is checked that upon projecting back to real space, the corresponding particle is not closer than d to any other particle for which the **q**-vector was already determined. In some instances it is not possible to place in all particles in a distance at least d from any other particle. Therefore we add a step, where we simply put in the last particles if they cannot be placed in without overlap.

1. Choose one particle in P as the initial particle. Find the **q**-vectors for particles in P, as described previously. However, only assign a bond to one of the twelve allowed directions if the bond deviates at most eight degrees from one of these twelve directions and if upon projecting back to real space, the corresponding particle does not overlap with one of the other particles for which the **q**-vector has already been determined.
2. Find the **q**-vectors for particles in R as in method 2, but only assigning a bond to one of the twelve allowed directions, if upon projecting back to real space, the corresponding particle does not overlap with one of the other particles for which the **q**-vector has already been determined.

3. Find the **q**-vectors for particles in D as in method 2, but only assigning a bond to one of the twelve allowed directions, if upon projecting back to real space, the corresponding particle does not overlap with one of the other particles for which the **q**-vector has already been determined.

4. Find the **q**-vectors for particles in D as in method 2.

3.4 Calculating diffusion coefficient

In order to find the diffusion coefficient of defects in a quasicrystal, one needs to track defects through a quasicrystal. The last method of the previous section can be used to classify the defect. As stated there, a defect consists those particles which are classified by this method to be a defect and which are connected. To associate a position to the defect, one can choose to take the center of mass of the particles composing the defect. Alternatively, one can choose to take the center of mass of the reference positions corresponding to the particles composing the defect. In this thesis we take the center of mass of the particles themselves as the position of a defect.
Now when tracking defects through the quasicrystal, we do not want to arbitrarily assign some index to each defect at every time step. Instead, we want to track which defect at time $t+1$ corresponds to which defect at time t. We briefly explain how this is done for a quasicrystal, assuming at least one at and most two defects. This may seem like a very strict requirement, but it is useful in certain cases.
Let $\mathbf{s}_i$, for $i \in \{1, \dots, n\}$, be the positions of the defects at one measurement and let $\mathbf{t}_j$, for $j \in \{1, \dots, m\}$, be the positions of the defects at the next measurement. First, for each $\mathbf{s}_i$, find $\mathbf{t}_j$ that is closest.

1. Let $\mathbf{x}_i^{t+1}$ be the positions of the defects at time $t+1$, in arbitrary order.

2. For each $i \leq n_t$, find

$$\mathrm{ind}_i = \arg \min_{1 \leq j \leq n_{t+1}} \left\| \mathbf{x}_j^{t+1} - \mathbf{s}_i^t \right\|, \tag{3.7}$$

   where $\left\| \mathbf{x}_j^{t+1} - \mathbf{s}_i^t \right\|$ indicates the distance between $\mathbf{x}_j^{t+1}$ and $\mathbf{s}_i^t$ using the nearest image convention, with periodic boundary conditions.

3. If $n_t = n_{t+1} = 2$, define

$$\mathbf{s}_i^{t+1} := \mathbf{x}_{\mathrm{ind}_i}^{t+1}. \tag{3.8}$$

   for $i \leq n_t$. We assume that the defects do not move too much such that $\mathrm{ind}_1^{t+1} \neq \mathrm{ind}_2^{t+1}$.

4. If $n_t = 1$ and $n_{t+1} = 2$, define

$$\mathbf{s}_1^{t+1} := \mathbf{x}_{\mathrm{ind}_1}^{t+1}, \tag{3.9}$$
$$\mathbf{s}_2^{t+1} := \mathbf{x}_{3-\mathrm{ind}_1}^{t+1}. \tag{3.10}$$

   This means that if a defect splits into two new defects, we assign the index 1 to the new defect that is closest to the old defect.

5. If $n_{t+1} = 1$, simply define

$$\mathbf{s}_1^{t+1} := \mathbf{x}_1^{t+1} \tag{3.11}$$

3.5 Diffusion coefficient

The diffusion coefficient of a particle is given by

$$D = \frac{\left\langle (\mathbf{r}(t) - \mathbf{r}(0))^2 \right\rangle}{2dt}, \tag{3.12}$$

where $r(t)$ is the position of the particle at time t and d is the number of dimensions and $\langle A \rangle$ is the expected value of quantity A. Let D_{free} be the diffusion coefficient of a free particle. Furthermore, let D be the diffusion coefficient of some particle. Then we define the relative diffusion coefficient of this particle as

$$D_r = \frac{D}{D_{\text{free}}} = \frac{\left\langle (\mathbf{r}(t) - \mathbf{r}(0))^2 \right\rangle}{\langle (\mathbf{r}_{\text{free}}(t) - \mathbf{r}_{\text{free}}(0))^2 \rangle}, \tag{3.13}$$

where $\mathbf{r}_{\text{free}}(t)$ is the position of a free particle at time t. We consider a Monte Carlo simulation, where at every step, a single particle is chosen and moved by some distance $\mathbf{dr}$ according to the Metropolis algorithm, where the components of $\mathbf{dr}$ are randomly uniformly chosen from an interval $[-\Delta, \Delta]$. In a Monte Carlo simulation, time is not well defined. However, we can still calculate a diffusion coefficient relative to the diffusion coefficient of a free particle. If the system consists of $N = 1$ free particle, then after k of such steps, the particle has a mean squared displacement of

$$\left\langle \mathbf{dr}^2_{\text{free}}(k) \right\rangle = \frac{dk\Delta^2}{12}. \tag{3.14}$$

In general, for a two dimensional system of N free particle, after k steps, particles have a mean squared displacement of

$$\left\langle \mathbf{dr}^2_{\text{free}}(k) \right\rangle = \frac{k\Delta^2}{6N}. \tag{3.15}$$

Now we can compute the diffusion coefficient of a defect relative to the diffusion coefficient of a free particle. Let $\left\langle \mathbf{dr}^2_{\text{def}}(k) \right\rangle$ be the measured mean squared displacement of a defect after k steps. Then the relative diffusion coefficient d_{def} of this defect is given by

$$d_r^{\text{def}} = \frac{\left\langle \mathbf{dr}^2_{\text{def}}(k) \right\rangle}{\left\langle \mathbf{dr}^2_{\text{free}}(k) \right\rangle} = \frac{6N \left\langle \mathbf{dr}^2_{\text{def}}(k) \right\rangle}{k\Delta^2}. \tag{3.16}$$

4 Results

4.1 Self-assembly of a quasicrystal

Figure 2.5 shows an equilibrium phase diagram for a two-dimensional system of hard-core soft-shoulder particles, with shoulder width $\delta = 1.4\sigma_{HD}$. This phase diagram shows that there is a small region where the system will form a quasicrystal. Therefore, the temperature and volume have to be chosen very precisely.
We ran a Monte Carlo simulation at a packing fraction of $\eta = 0.77$ and reduced temperature $T^* = 0.37$, with $N = 500$ particles. The system was initialized as a fluid. Some snapshots of this simulation are shown in Figure 4.1, with Figure 4.1a taken shortly after the simulation started, and 4.1b and 4.1c taken after the system has equilibrated. Clearly, the structure that appears shortly after the simulation starts (Figure 4.1a) contains a high number of defects. In between defects, the particles mostly have a hexagonal crystal structure, although there are some regions of a square crystalline structure. In the end, as shown in Figures 4.1b and 4.1c, the structure appears more quasicrystalline in nature and the number of defects has reduced, although several still remain. Figure 4.1d shows the edges drawn between neighboring particles, for the configuration in Figure 4.1c. This clearly shows a square-triangle tiling, with defects. Note that the relatively large number of defects, even in the equilibrated snapshots, was seen in nearly all the cases where we explored the self-assembly. Hence, in order to understand the structure of the self-assembled quasicrystal, it is important to be able to identify and characterize the defects.

4.2 Vacancy defects

To study defects in a quasicrystal in a controlled manner, we start with a 'perfect' quasicrystal. In this context, a perfect quasicrystal is a configuration of particles in a finite box, subject to periodic boundary conditions, such that there are no defects present. This perfect quasicrystal functions as a starting point. We can now introduce a defect by either removing a particle from the system, or adding a particle to the system, and exploring how the quasicrystalline structure reacts to these changes.
We start by removing a particle from a perfect quasicrystalline lattice. Depending on which particle is removed from the lattice, the result is one of the four configurations shown in Figure 4.2, up to a rotation. Naturally, removing a particle from the system leaves a gap. When the system evolves, a particle will eventually move into this gap. As one particle moves halfway into the gap, two separate smaller gaps are left. Examples of this are shown in Figure 4.3. From here, three things can happen. Firstly, the particle in question can return to its original position, which returns the system to its starting configuration. Secondly, the particle in question can continue to move in the same direction, filling the original gap and leave a gap at the original position of the particle, again resulting in one of the four configurations shown in Figure 4.2. Last of all, one of the other particles adjacent to one of the two smaller gaps can move towards such a smaller gap. As a result, the two separate gaps move away from each other. In this way, two defects can completely separate themselves from each other. Interestingly, at high enough densities, these separate defects are found in just two configurations, which are shown in Figure 4.4.
If the two gaps continue to move away from each other, they are eventually separated by non-defect particles. Once this happens, the single defect has split into two separate defects – each associated with half the missing particle. These separate defects are able to move through the quasicrystal.
Using method II (see Subsection 3.3.2) we were able to find a reference lattice for particles in the quasicrystal. The result is shown in Figure 4.5. Here the smaller red and green dots form the reference lattice. Furthermore, the green dots are defects in the lattice. This Figure shows that the particles coincide very well with their reference positions. This is also true for the defect particles. We see furthermore that the defects found by method I, i.e. the purple particles, and the defects found by method II, i.e. the green lattice points, do not match. This is because method I is more sensitive to changes caused by thermal fluctuations in the lattice, which do not fundamentally change the structure of the underlying lattice. In method II, these thermal fluctuations are filtered out.

4.3 Diffusion of vacancy defects

By looking at the reference points on the lattice, we can track the defects moving through the quasicrystal. Figure 4.6a shows the paths of two defects. Notice that the defects only move in twelve different directions.

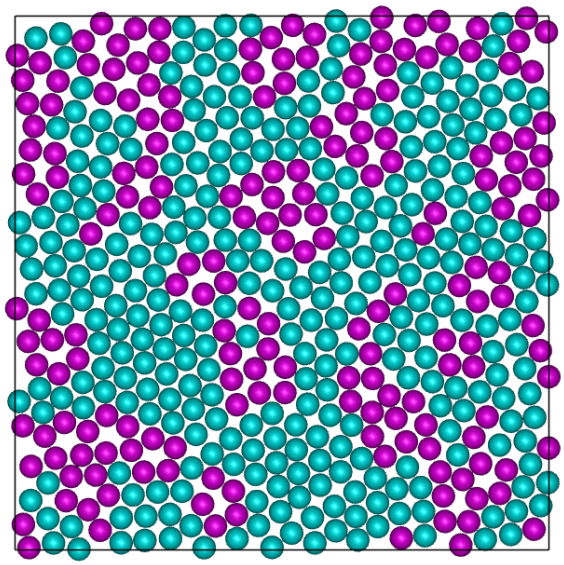

(a) Core-corona system shortly after initialization.

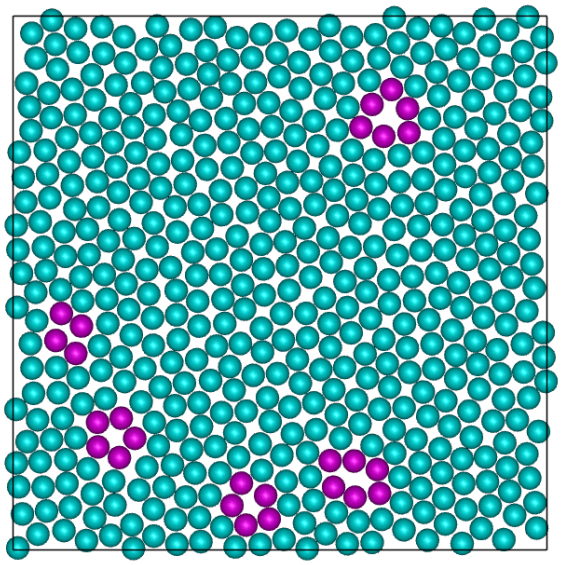

(b) The same system after equilibration.

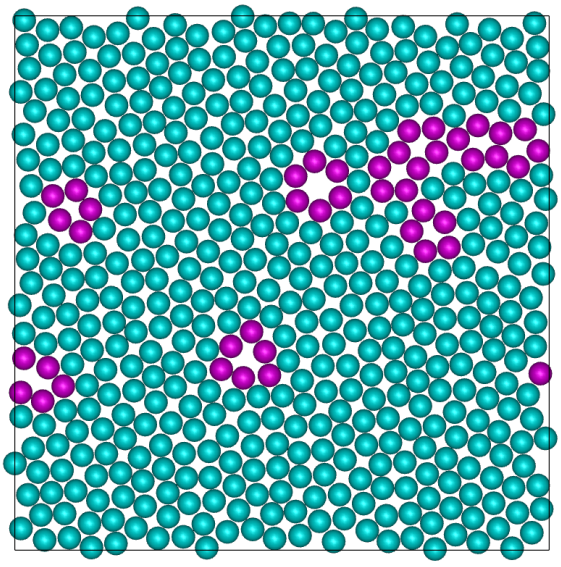

(c) The even longer after equilibration.

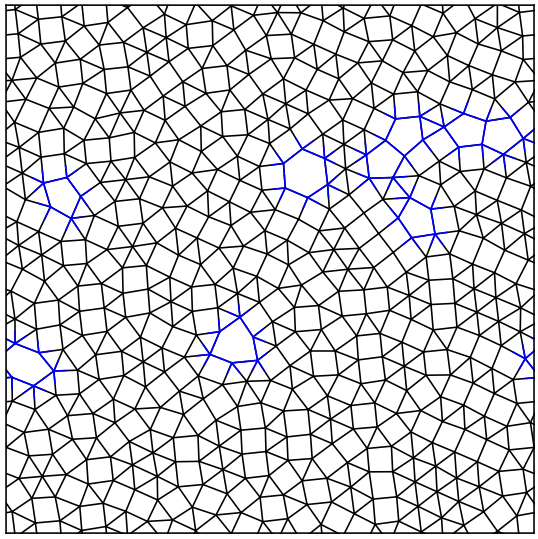

(d) Bonds corresponding to snapshot 3. Half edges from an edge are colored blue if the corresponding particle is classified as a defect by the method as described in 3.3.

Figure 4.1: Snapshots of a Monte Carlo simulation of 500 core corona particles at $\eta = 0.78$ and $T^* = 0.37$. Particles are colored purple if they are classified as a defect, using the method as described in section 3.3.

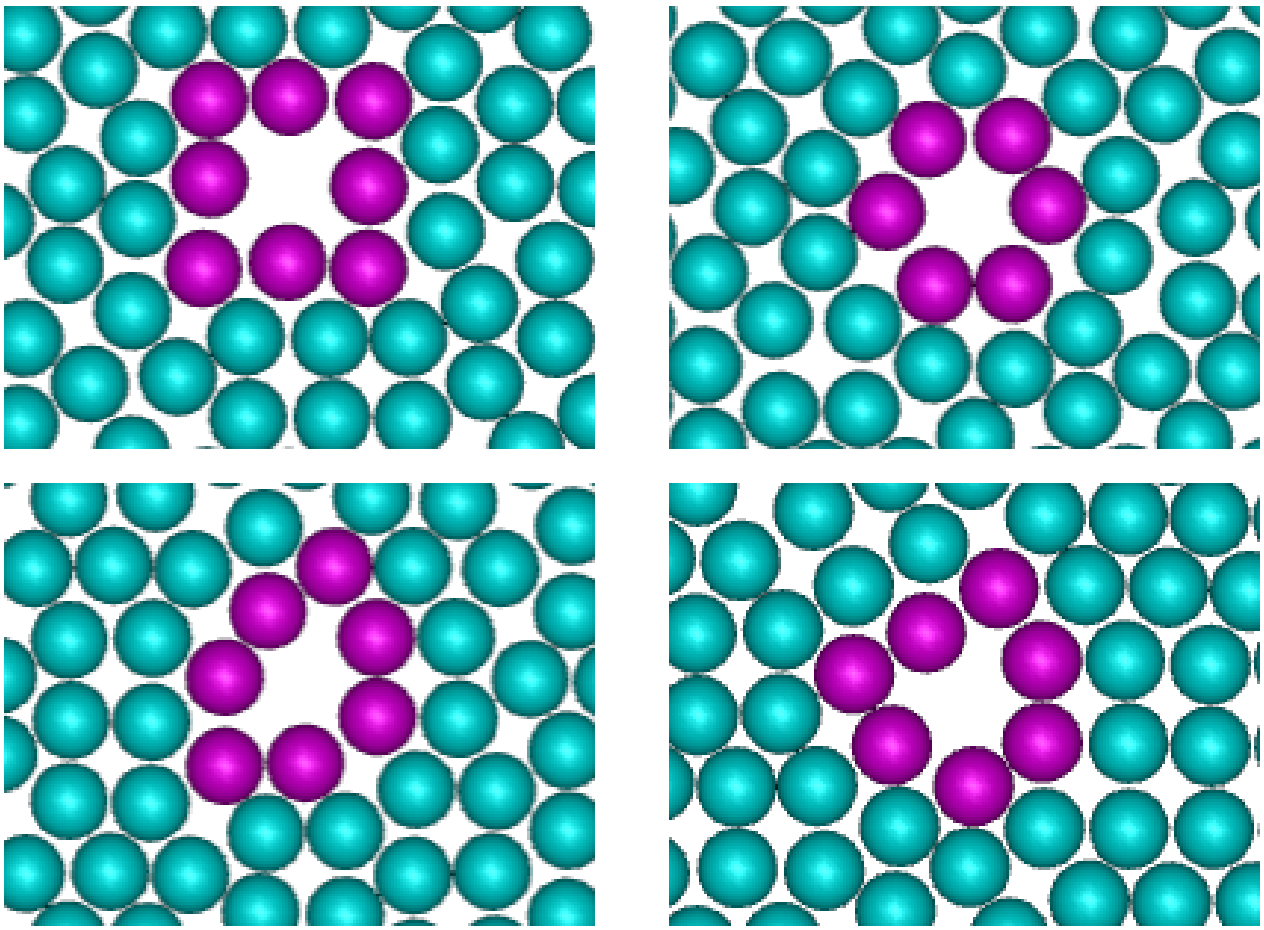

Figure 4.2: Possible configurations after removal of a particle.

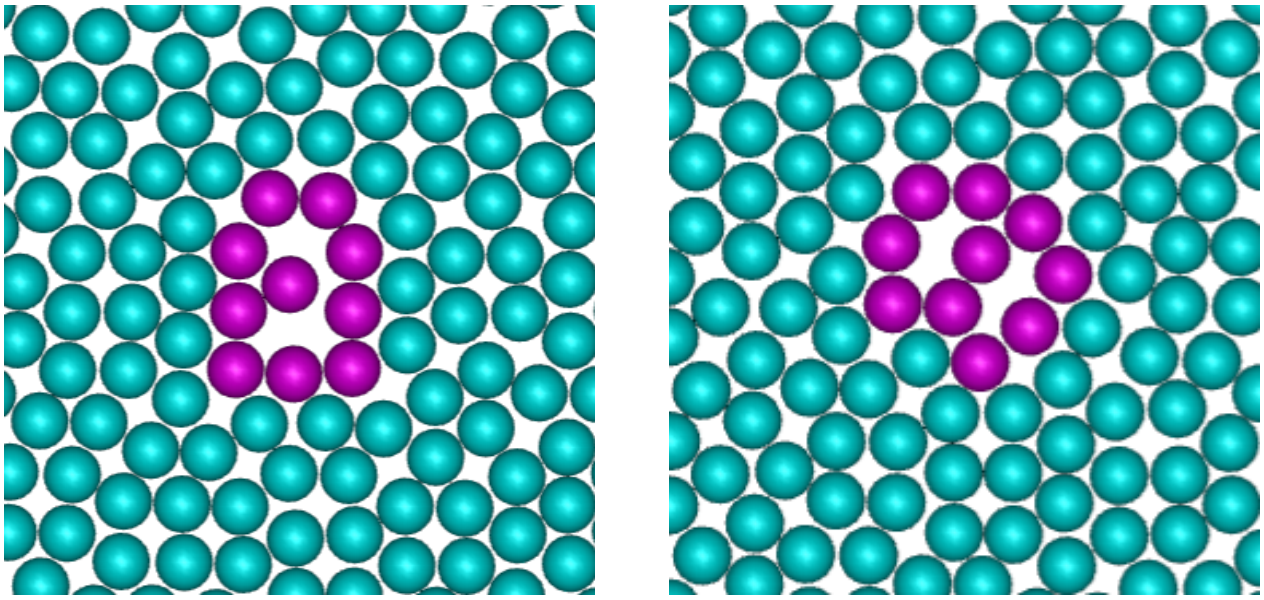

Figure 4.3: Configurations where a particle has moved halfway into a vacancy, leaving two half vacancies.

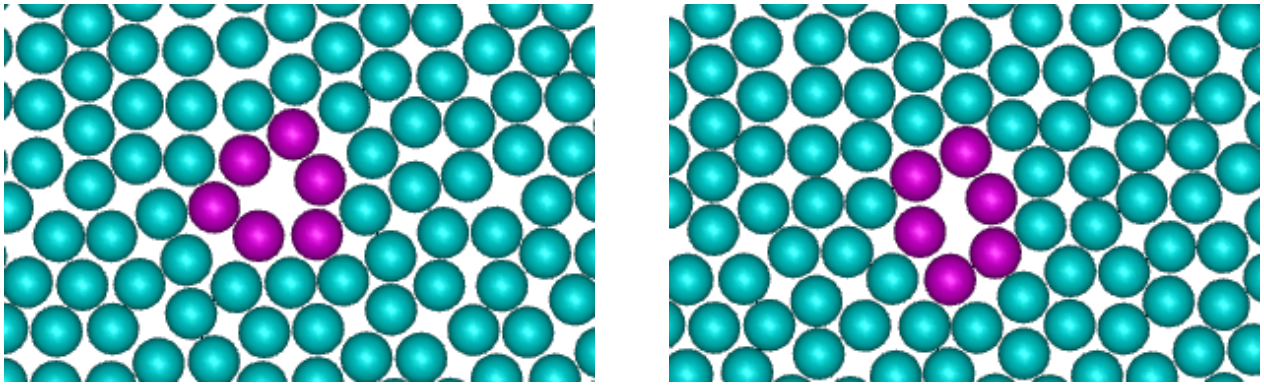

(a) Shield defect. (b) Egg defect.

Figure 4.4: Possible configurations of split defects.

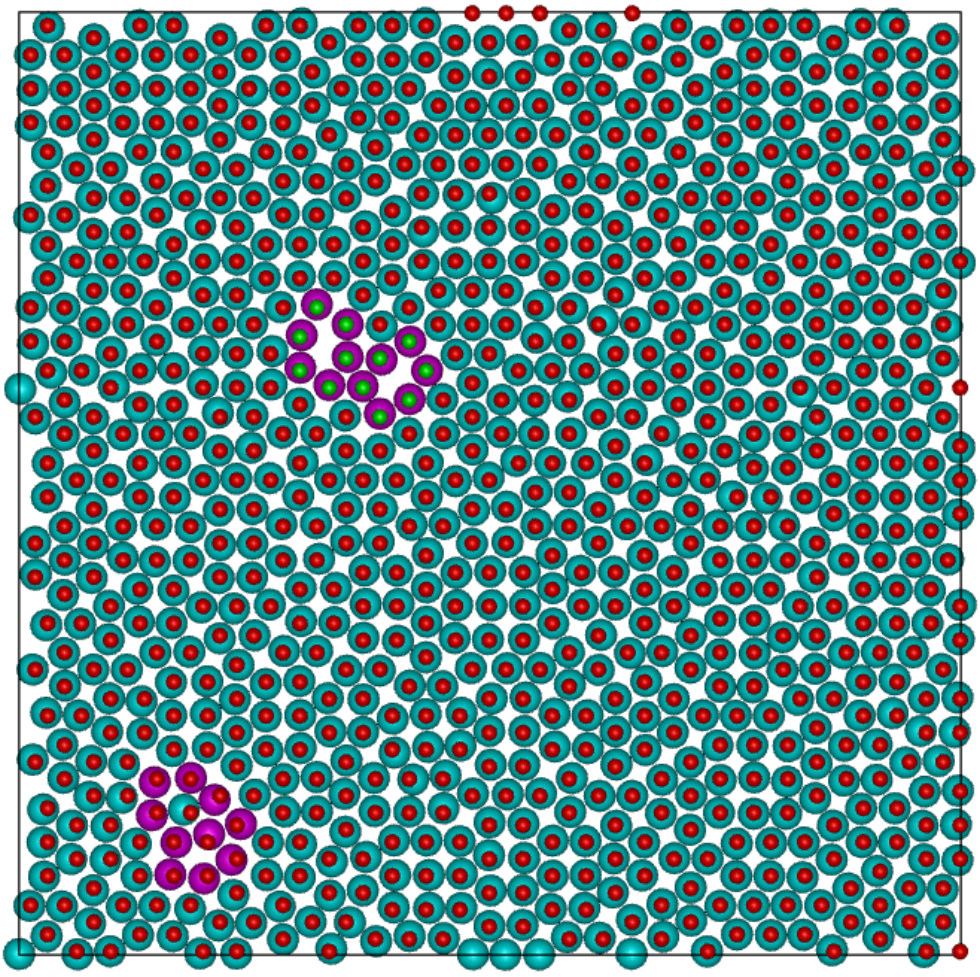

Figure 4.5: Snapshot of the quasicrystal at packing fraction $\eta = 0.77$ and reduced temperature $T^* = 0.35$. The purple particles are the particles which are characterized as a defect by method 1. The green particles are the lattice points that are characterized as a defect.

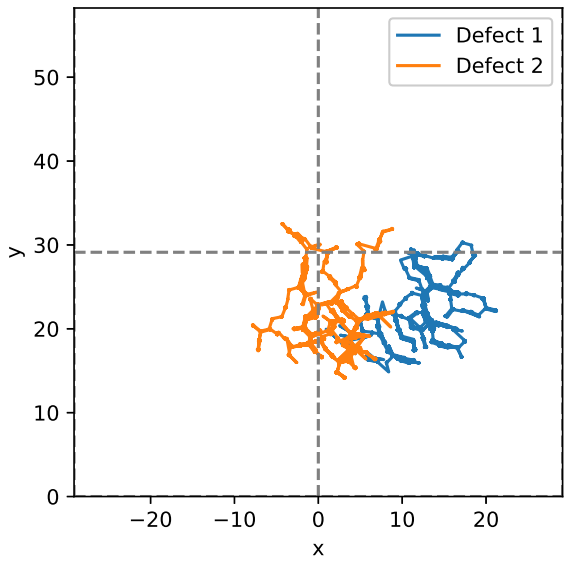

(a) The path of the two defects traced by the two defects for packing fraction 0.774 and reduced temperature $T^* = 0.37$. Notice the defects move in only twelve directions, barring a random walk of the lattice itself.

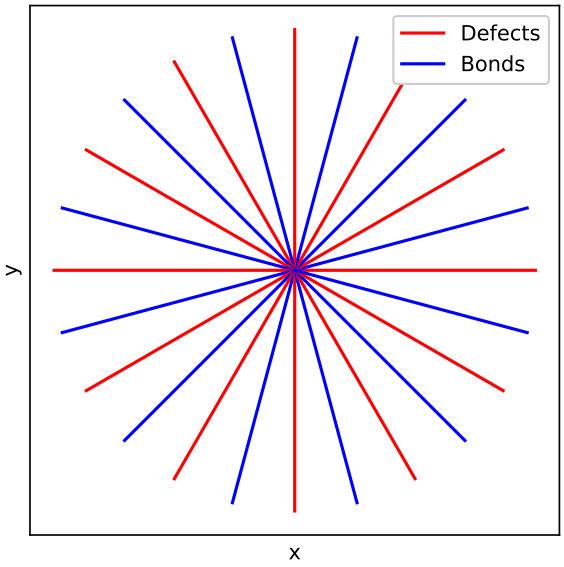

(b) The red lines signify the allowed directions of bonds between particles. The blue lines indicate the directions in which the defect is able to move.

These twelve directions do not coincide with the directions of the bonds between particles. Instead, the directions in which the defects move have an angle difference with the bonds of 15 degrees (see Figure 4.6b). Figure 4.7 shows the diffusion coefficient of the vacancy defects as a result of the packing fraction for different temperatures. For lower packing fractions, the diffusion coefficient was not measured, due to spontaneous forming of new defects. The method described in this thesis does not work correctly if additional defects form. Therefore we were not able to measure the diffusion coefficient for packing fractions lower than 0.770. As one might expect, the diffusion coefficient is higher at higher temperatures. Furthermore, the diffusion decreases as the packing fraction increases. At all temperatures, the diffusion coefficient at packing fraction 0.770 is about twice as high as at packing fraction 7.798.

4.4 Interstitial defects

We now examine the behavior of interstital defects. We initialized a perfect quasicrystal at $T^* = 0.37$ and packing fraction $\eta = 0.78$. We inserted an additional particle into the system. Figure 4.8 shows the system right after the insertion of an extra particle. The inserted particle introduces a defect into the quasicrystal. Figure 4.9 shows some snapshots of this same simulation. Compared with a vacancy defect, it is much harder to describe what happens with an interstitial defect. Immediately after insertion of an extra particle the particles around the inserted particles are pushed away. This deforms the underlying quasicrystal lattice and introduces a defect. As the quasicrystal evolves, this usually leads to pentagons forming in the quasicrystal. The defects in the reference lattice does not always seem to coincide very well with the visual position of the defects, see e.g. Figure 4.9c. Additionally, the defects in the lattice seem to move around more from time step to time step than for the vacancy defect. This can be partly explained by the inherent randomness of the method to obtain this reference lattice. The position of every lattice point is e_i, relative to one of its neighboring lattice points, for $i \in \{1, \ldots, 12\}$. Around the defects, it matters in which order lattice points are assigned a position. This means the position of the defect in the lattice is dependent on this order. As a result, in contrast to the vacancy defects, interstitial defects do not have a well defined position. Due to the interstitial defects not having a well defined position we were not able to do a diffusion study on the interstitial defects.

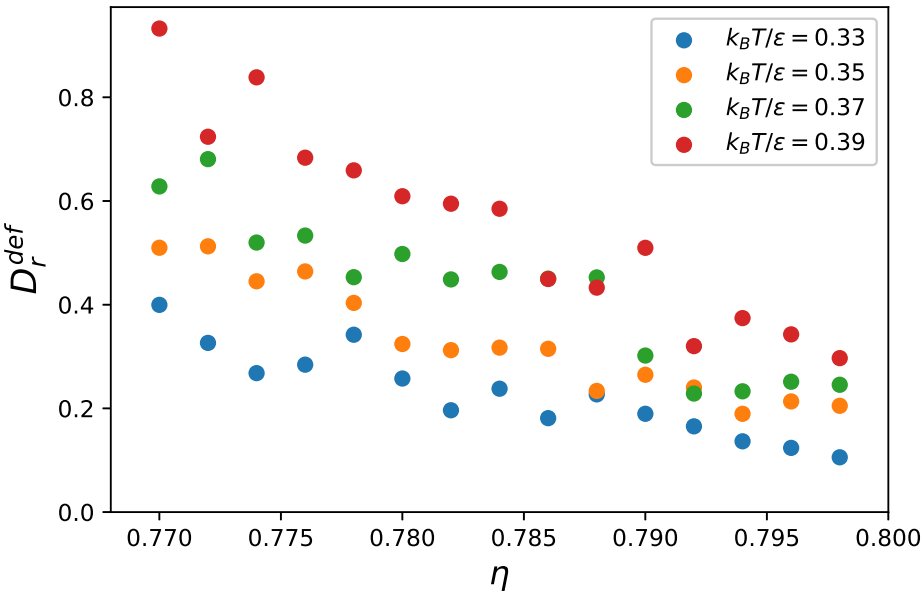

Figure 4.7: Diffusion coefficient as function of the packing fraction for four different reduced temperatures. This result clearly shows that the diffusion coefficient decreases as the packing fraction increases, while the diffusion coefficient increases as the temperature increases.

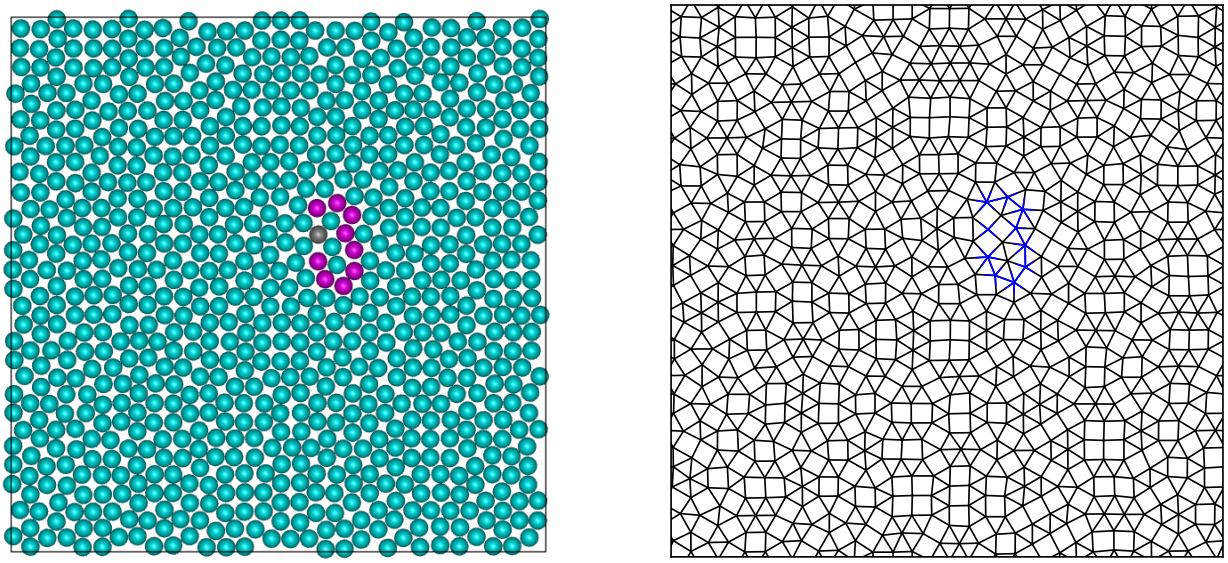

(a) Quasicrystal just after insertion of a particle. The inserted particle is colored gray.

(b) Corresponding bonds drawn between neighboring particles.

Figure 4.8: Quasicrystal without defects right after insertion of an extra particle.

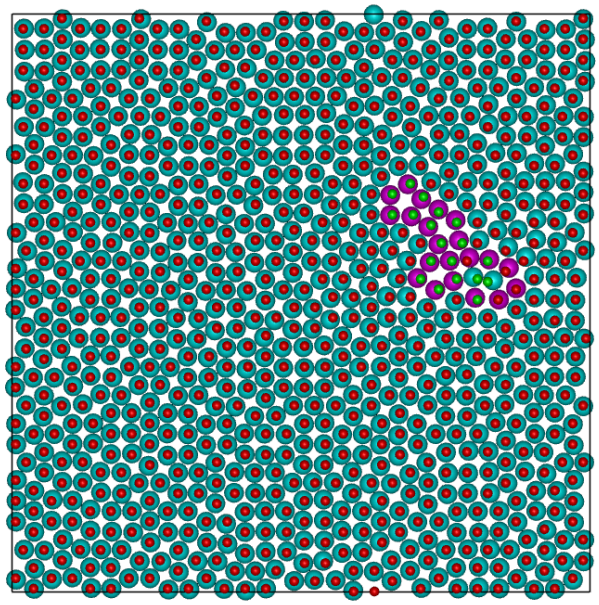

(a) Snapshot of simulation of interstitial.

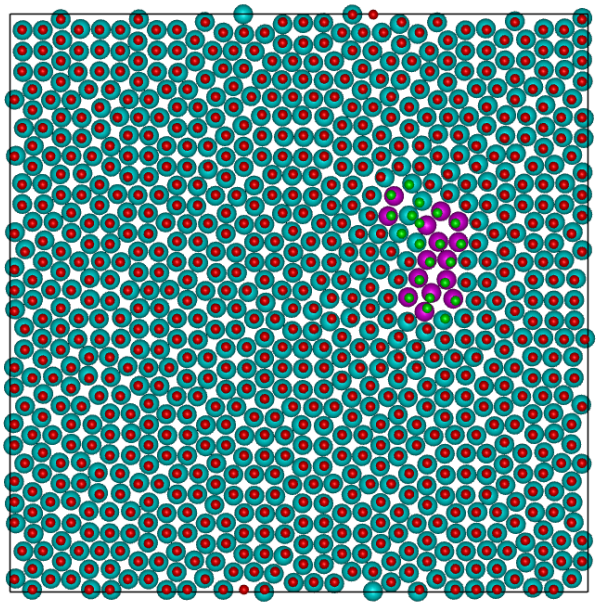

(b) Snapshot of simulation of interstitial.

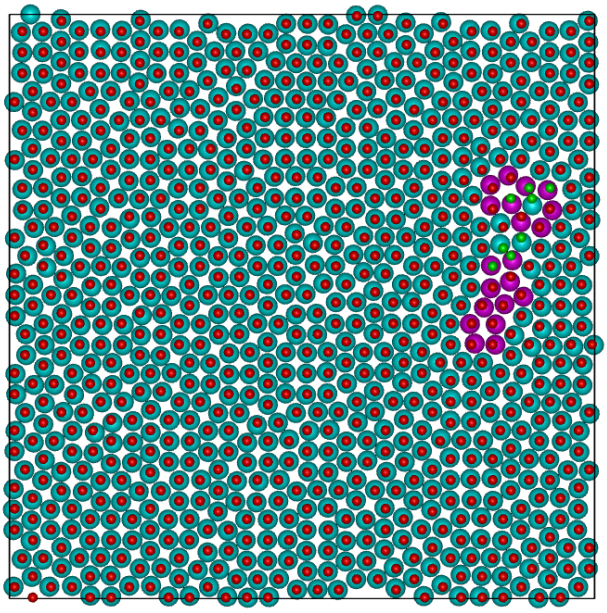

(c) Snapshot of simulation of interstitial.

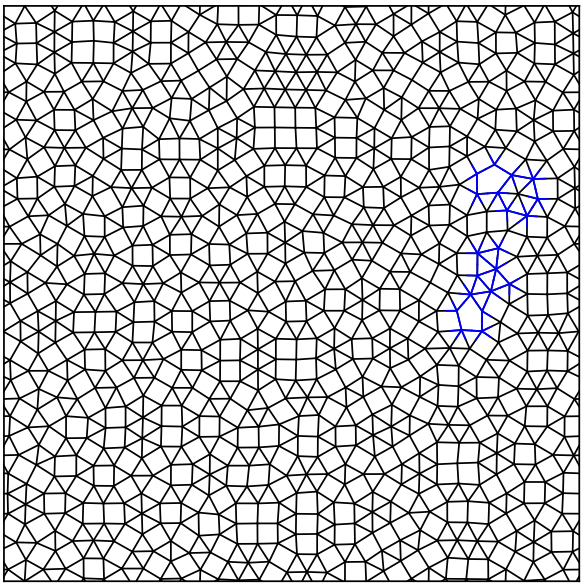

(d) Bonds corresponding to Figure 4.9c.

Figure 4.9: Snapshots of simulation of interstitial at packing fraction $\eta = 0.78$ and reduced temperature $T^* = 0.37$. The red and green disks represent the reference lattice. The green disks are defects in the lattice.

4.5 Conclusion

We have shown that core corona particles with a shoulder of $\delta = 1.4\ \sigma_{\mathrm{HD}}$ self assemble into a quasicrystal for the right reduced temperature and density. We found that some defects remained in this quasicrystal.
We developed a method which can be used to track the vacancy defects at a high enough packing fraction, i.e. $\eta > 0.70$. For lower packing fractions fluctuations would sometimes cause particles to stray too much from their reference positions, which causes the method for locating defects to recognize this fluctuation as a defect. Future research may be done to perfect the method, such that it also works for lower densities.
We have used the developed method to track vacancy defects through a quasicrystal and calculate their diffusion coefficient for different packing fractions and temperatures. Unsurprisingly, we found that the diffusion coefficient decreased as the packing fraction increased. Similarly, the diffusion coefficient increased as the temperature increased.
Additionally, we have used the developed method of finding a reference lattice for the particles to look at interstitial defects. We found that interstitial defects have much more diverse behaviour. Furthermore, the reference lattice is too sensitive to inherent randomness to use it to find well defined positions of the interstitial defects. For this reason we were not able to to a diffusion study on the interstitial defects.
In future studies, one might circumvent this problem by taking a much larger system and letting it evolve for longer. In this way, the fluctuations can be rendered small enough at larger time scales. This was however outside of the scope of this thesis.

PART II

CALCULATING PHOTONIC PROPERTIES OF A QUASICRYSTAL

5 Theory

5.1 Maxwell's equations

To see how light propagates through a colloidal quasicrystal, we need to solve Maxwell's equations on this quasicrystal. Approximate solutions can be found using numerical methods. Performing the calculations, that are needed in order to study the photonic properties of a quasicrystal, is difficult to implement in two dimensions. Therefore, we will instead consider a one dimensional quasicrystal, for which the mathematical challenges of solving Maxwell's equations are similar, but the numerical and implementation challenges are much easier to tackle.
Similar to a two dimensional quasicrystal, a one dimensional quasicrystal consists of subpatterns that are repeated aperiodically, as in Figure 5.1. Each subpattern consists of some number of slabs, indicated by gray and blue regions in Figure 5.1. These slabs are analogous to colloids and the solvent in a quasicrystal. In colloids, the dielectric constant ϵ_r is usually different than in the solvent. By analogy, we assume that different slabs have a different dielectric constant. Furthermore, we assume that the dielectric constant is constant on each slab and the magnetic permeability in the slabs is equal to that in free space.
In general, we assume that there is a number p, of different patterns of slabs, where all slabs are nonmagnetic. On each of these patterns, the dielectric coefficient is piecewise constant in the z direction. Furthermore, we assume that the dielectric coefficient has no x or y dependence. Outside of these slabs, we assume that there is vacuum, meaning that there we have $\epsilon_r = 1$.
In Section 1.3, we showed that assuming that the magnetic field is time harmonic with frequency ω, Maxwell's equations lead to

$$\nabla \times \left(\frac{1}{\epsilon_r} \times \mathbf{H} \right) = \left(\frac{\omega}{c} \right)^2 \mathbf{H}. \tag{5.1}$$

We assume that the magnetic field is independent of the x and y coordinates. We consider that $\mathbf{H}$ is polarized in the x direction. Using this, Equation 5.1 reduces to

$$\nabla \times \frac{1}{\varepsilon_r} \nabla \times (H_x, 0, 0) = \nabla \times \frac{1}{\varepsilon_r} \left(0, \frac{\partial H_x}{\partial z}, 0 \right) = - \left(\frac{\partial}{\partial z} \frac{1}{\epsilon_r} \frac{\partial H_x}{\partial z}, 0, 0 \right) = \left(\frac{\omega}{c} \right)^2 (H_x, 0, 0). \tag{5.2}$$

We have reduced the three-dimensional Maxwell equations to a one-dimensional Helmholtz equation:

$$-\frac{\partial}{\partial z} \frac{1}{\epsilon_r} \frac{\partial H}{\partial z} = \left(\frac{\omega}{c} \right)^2 H, \tag{5.3}$$

where we drop the x subscript.

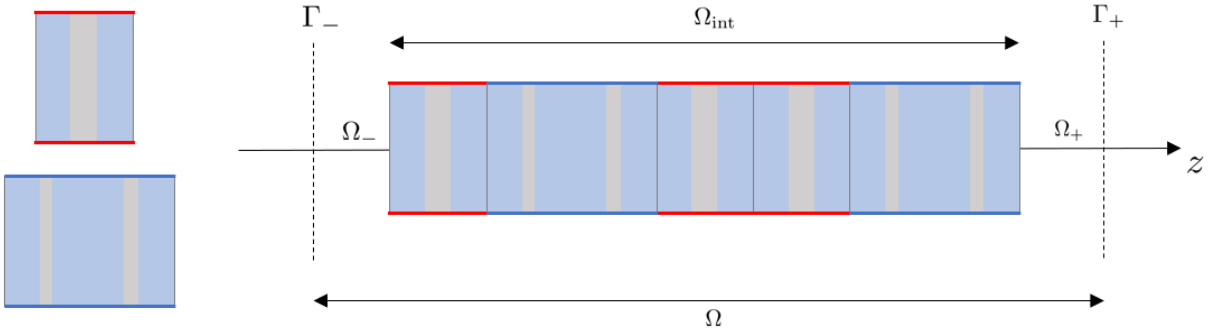

Figure 5.1: Schematic representation of the quasicrystalline stack. On Ω_- and Ω_+, there is vacuum and therefore $\varepsilon_r = 1$. Subpatterns (left) are combined to form the stack (right).

5.2 Boundary conditions

There is a vacuum in Ω_- and Ω_+. In these regions we have $\epsilon_r = 1$. For $\epsilon_r = 1$, (5.3) reduces to a one dimensional wave equation. This means that locally the solution must be a superposition of left and right travelling wave. Therefore, locally the solution must be of the form

$$H(z,t) = H_{\mathrm{r}}(z - ct) + H_{\mathrm{l}}(z + ct), \tag{5.4}$$

for some functions $H_{\mathrm{r}}, H_{\mathrm{l}}$. These functions correspond to the right and left travelling wave respectively. From (2.6) we can see that $H(z,t) = \hat{H}(z)e^{-i\omega t}$ for some $\hat{H}$, which should be a solution to (5.3). That means that

$$\hat{H}(z) = H_{\mathrm{r}}(z - ct)e^{i\omega t} + H_{\mathrm{l}}(z + ct)e^{i\omega t}. \tag{5.5}$$

Since $\hat{H}(z)$ has no time dependence, taking the time derivative must yield zero.

$$\frac{\partial \hat{H}(z)}{\partial t} = \left[i\omega H_{\mathrm{r}}(z - ct) - cH'_{\mathrm{r}}(z - ct)\right] e^{i\omega t} + \left[i\omega H_{\mathrm{l}}(z + ct) + cH'_{\mathrm{l}}(z + ct)\right] e^{i\omega t} = 0. \tag{5.6}$$

We can divide out $e^{i\omega t}$ and we can vary $z - ct$ and $z + ct$ independently. This gives

$$\begin{cases} i\omega H_{\mathrm{r}}(z - ct) - cH'_{\mathrm{r}}(z - ct) = 0, \\ i\omega H_{\mathrm{l}}(z + ct) + cH'_{\mathrm{l}}(z + ct) = 0. \end{cases} \tag{5.7}$$

Solving this differential equation and inserting the solutions for H_{r} and H_{l} into (5.5), and evaluating at $t = 0$ yields

$$\hat{H}(z) = H_{\mathrm{r}}(z) + H_{\mathrm{l}}(z), \qquad \text{with } H_{\mathrm{r}}(z) = A^{\mathrm{r}}e^{ikz} \text{ and } H_{\mathrm{l}}(z) = A^{\mathrm{l}}e^{-ikz}. \tag{5.8}$$

where $k = \omega/c$ is the wave number and $A^{\mathrm{l}}, A^{\mathrm{r}} \in \mathbb{C}$. The superscripts l and r refer to the left and right travelling wave, respectively. We are modelling an incoming wave from the left. This means that on Ω_-, we need to impose this right travelling wave. Since there is no left travelling wave coming from the right, we need to impose that there is no left travelling wave in Ω_+. This can be done by using Robin boundary conditions. From (5.8) we can see that on Ω_-, we have

$$\frac{\partial \hat{H}(z)}{\partial z} + ik\hat{H}(z) = (ik + ik)\, A^{\mathrm{r}}e^{ikz} + (-ik + ik)\, A^{\mathrm{l}}e^{-ikz} = 2ikA^{\mathrm{r}}e^{ikz} \tag{5.9}$$

Similarly, on Ω_+, we have

$$\frac{\partial \hat{H}(z)}{\partial z} - ik\hat{H}(z) = (ik - ik)\, A^{\mathrm{r}}e^{ikz} + (-ik - ik)\, A^{\mathrm{l}}e^{-ikz} = -2ikA^{l}. \tag{5.10}$$

Since there is no incoming left travelling wave from the left we set $A^l = 0$ on Ω_+. We obtain the boundary conditions

$$\begin{cases} \frac{\partial \hat{H}(z)}{\partial z} + ik\hat{H}(z)\Big|_{\Gamma_-} = A, \\ \frac{\partial \hat{H}(z)}{\partial z} - ik\hat{H}(z)\Big|_{\Gamma_+} = 0, \end{cases} \tag{5.11}$$

where $A = 2ikA^r e^{ikz}\big|_{\Gamma_-}$. Without loss of generality, we can assume that A is real.
In conclusion, we need to solve the following model:

$$\begin{cases} -\frac{\partial}{\partial z}\frac{1}{\epsilon_r}\frac{\partial \hat{H}}{\partial z} = \left(\frac{\omega}{c}\right)^2 \hat{H}, & \text{on } \Omega, \\ \frac{\partial \hat{H}}{\partial z} + ik\hat{H}\Big|_{\Gamma_-} = A, & \text{at } \Gamma_-, \\ \frac{\partial \hat{H}}{\partial z} - ik\hat{H}\Big|_{\Gamma_+} = 0, & \text{at } \Gamma_+. \end{cases} \tag{5.12}$$

5.3 Difficulties

In the next chapter, we develop a finite elements method to approximate a solution to (5.12). However, it turns out that the term $\left(\frac{\omega}{c}\right)^2 H$ makes the analysis more difficult. This term makes it more difficult to prove convergence of our method. For the purposes of developing our method, we replace the term $\left(\frac{\omega}{c}\right)^2 H$ by a source term f. Furthermore we replace the boundary conditions by homogeneous Dirichlet boundary conditions. We obtain

$$\begin{cases} -\frac{\partial}{\partial z}\frac{1}{\epsilon_r}\frac{\partial \hat{H}}{\partial z} = f, & \text{on } \Omega, \\ \hat{H} = 0, & \text{at } \Gamma_-, \\ \hat{H} = 0, & \text{at } \Gamma_+. \end{cases} \tag{5.13}$$

In [30], it is shown that finite elements solutions of the one dimensional Helmholtz equation do converge. This indicates that a finite elements method that works for the simplified problem (5.13) may also work for the more physical problem (5.12).

6 finite element method

In this section we describe two finite element methods that can be used to approximate the solution to (5.13). We first describe the geometry of the problem in mathematical terms.

6.1 Geometry of the quasicrystal

We are considering a problem on the interval $\Omega := (0, L)$, which is partitioned into cells C_i. I.e.

$$\bar{\Omega} = \bigcup_{i=1}^{n} \bar{C}_i, \qquad C_i = (z_{i-1}, z_i), \tag{6.1}$$

for some partition $0 = z_0 < z_1 < \ldots < z_n = L$. We are assuming that there are p unit cells $\hat{C}_j = (0, \bar{c}_j)$, with $p \ll n$. To each unit cell $\hat{C}_j$, a piecewise constant function $a_j : \hat{C}_j \to \mathbb{R}$ is associated. Each cell C_i corresponds to some unit cell $\hat{C}_j$. Let T be the function that maps the index i to index j if cell C_i corresponds to unit cell $\hat{C}_j$. Then we define the function

$$a(z) = a_{T(i)}(z - z_{i-1}) \quad \text{for } z \in C_i. \tag{6.2}$$

This function a is related to the dielectric coefficient via $a(z) = 1/\varepsilon(z)$. The functions a_j describe the dielectric coefficient of each slab in the stack. We assume that a bound $C \in \mathbb{R}$ exists such that

$$0 < \frac{1}{C} \leq a(z) \leq C. \tag{6.3}$$

Furthermore, we denote the discontinuities in a by x_i for $i \in \{1, \ldots, P\}$, with $x_i < x_{i+1}$. We define $\mathcal{P}$ to be the discontinuity set of a, i.e.

$$\mathcal{P} := \{x_i, : i \in \{1, \ldots, P\}\}. \tag{6.4}$$

6.2 Weak formulation and analysis

This section mostly follows an analysis by Brenner and Scott [31]. Consider the following problem. Find the solution u to

$$-(a(z)u'(z))' = f(z), \quad \text{for } z \in (0, L), \quad u(0) = u(L) = 0, \tag{6.5}$$

where a is a piecewise constant function. Moreover, we assume that $f \in L^2(0, L)$. Notice that this problem is similar to (5.12). However, the $\left(\frac{\omega}{c}\right)^2 \bar{H}$ term is left out. Furthermore, the Robin boundary conditions are replaced by homogeneous Dirichlet boundary conditions. We can rewrite this problem in the weak formulation. If v is any sufficiently regular function such that $v(0) = v(L) = 0$, then integration by parts yields the weak form of the problem

$$\text{Find } u \in H_0^1 \text{ such that } b(u, v) = (f, v), \quad \forall v \in H_0^1, \tag{6.6}$$

where the space H_0^1 is defined by

$$H_0^1 = \left\{ v \in L^2(0, L) : \int_0^L a(v')^2 \, dz < \infty \text{ and } v(0) = v(L) = 0 \right\}. \tag{6.7}$$

and we have the bilinear form

$$b(u, v) := \int_0^L a u' v' \, dz \tag{6.8}$$

and the inner product

$$(f, v) := \int_0^L f v \, dz. \tag{6.9}$$

The H^1 norm is defined as

$$\|v\|_{H^1} := \sqrt{(v,v)+(v',v')}. \tag{6.10}$$

Notice that for any $u \in H_0^1$, the boundary conditions are met. We will see that (6.6) has a unique solution. First we note that any $u \in H_0^1$ is continuous.

Lemma 6.2.1. *Let $u \in H_0^1$. Then u is continuous on $[0,L]$.*

Proof. If u is a solution to (6.6), then $u \in H^1(0,L) = W^{1,2}(0,L)$. Morrey's lemma (see Ref. [32, Chapter 5.6, Theorem 5]) states that for a bounded open subset $U \subset \mathbb{R}$, with $\partial U \in C^1$, we have

$$\|u\|_{C^{0,\gamma}(\bar{U})} \leq K\|u\|_{W^{1,p}(U)}, \tag{6.11}$$

with $\gamma = 1 - n/p$, for some real constant $K > 0$. Then

$$\|u\|_{C^{0,1/2}[0,L]} \leq K\|u\|_{W^{1,2}(0,L)} < \infty, \tag{6.12}$$

That means that u is Hölder continuous on $[0,L]$ and therefore u is continuous on $[0,L]$. □

To show uniqueness and existence, we use a lemma introduced by Lax and Milgram and was further generalized by Babuška in 1971 [30]. The following is a special case of this lemma.

Lemma 6.2.2 (Lax-Milgram)**.** *Let H be a Hilbert space. Furthermore, let $B(u,v)$ be a bounded bilinear form on $H \times H$, $u, v \in H$, which is continuous*

$$B(u,v) \leq \alpha\|u\|_H\|v\|_H. \tag{6.13}$$

and strongly coercive, i.e.

$$|B(u,u)| \geq \beta\|u\|_H^2, \tag{6.14}$$

for some constants $\alpha, \beta > 0$ and all $u \in H$. Furthermore, let $g \in H'$, i.e. g be a linear functional on H. Then there exists exactly one element $u_0 \in H$ such that

$$B(u_0, v) = g(v), \tag{6.15}$$

for all $v \in H$.

We can apply this lemma to the problem of (6.6) to show that it has a unique solution. This result is captured in the following theorem.

Theorem 6.2.3. *There exists a unique solution $u_0 \in H_0^1$ for (6.6).*

Proof. We use Lemma 6.2.2 to prove this theorem. We first need to show that the assumptions of that lemma hold. Therefore we need to show that the bilinear form b is continuous and coercive. Continuity follows from the Cauchy Schwarz inequality:

$$b(u,v) \leq C\int_0^L |u'||v'|\,dz \leq C \cdot \sqrt{(u',u')}\sqrt{(v',v')} \leq C \cdot \|u\|_{H^1(0,L)}\|v\|_{H^1(0,L)}. \tag{6.16}$$

Using that $u(0) = 0$ in combination with the Cauchy Schwarz inequality, we find that b is strongly coercive:

$$\begin{aligned}\int_0^L u^2\,dz &= \int_0^L \left(\int_0^z u'(t)\,dt\right)^2 dz \leq \int_0^L \left(\int_0^L u'(t)\cdot 1\,dt\right)^2 dz \\ &\leq \int_0^L \left(\int_0^L |u'(t)|^2\,dt \int_0^L |1|^2\,ds\right) dz = L^2\int_0^L |u'|^2 dz \leq CL^2 b(u,u),\end{aligned}$$

so $b(u,u) \geq CL^2\|u\|_{L^2}^2$. Additionally, we have used here that $a(z) < C$, for $z \in [0,L]$. Now last of all, we can define g to be the functional

$$g(u) := (f,u). \tag{6.17}$$

By bilinearity of the inner product, g is a linear functional. g is also continuous, since

$$g(u) = (f,u) \leq \sqrt{(f,f)}\sqrt{(u,u)} \leq \|f\|_{L^2(0,L)}\|u\|_{H^1(0,L)}. \tag{6.18}$$

Since b is a continuous, strongly coercive bilinear form and g is a linear continuous functional, we can apply Lemma 6.2.2, to find there exists a unique solution $u_0 \in H_0^1$, such that

$$b(u_0,v) = g(v) = (f,v), \tag{6.19}$$

for all $v \in H_0^1$. □

Lemma 6.2.4. *For $i \in \{1,\dots,P-1\}$, let $f\big|_{(x_i,x_{i+1})} \in H^m(x_i,x_{i+1})$. Then $u\big|_{(x_i,x_{i+1})} \in H^{m+2}(x_i,x_{i+1})$.*

Proof. Observe that a is constant on the intervals (x_i,x_{i+1}) and therefore $a\big|_{(x_i,x_{i+1})} \in C^\infty(x_i,x_{i+1})$. The desired result follows from [32, Ch. 6.3, Theorem 2]. □

Corollary 6.2.5. *For $i \in \{1,\dots,P-1\}$, let u be the solution to (6.6). Then u is regular on all intervals (x_i,x_{i+1}), for $i \in \{1,\dots,P-1\}$.*

Proof. Since $f \in L^2(0,L)$, it follows that $f\big|_{(x_i,x_{i+1})} \in L^2(x_i,x_{i+1}) = H^0(x_i,x_{i+1})$. By Lemma 6.2.4 it follows that $u\big|_{(x_i,x_{i+1})} \in H^2(x_i,x_{i+1})$. □

6.3 Ritz-Galerkin approximation

Finding a solution to (6.6) is no trivial matter. Therefore, let us approximate the problem. We consider a closed subspace $S \subset H_0^1$ and consider the Galerkin approximation of (6.6):

$$\text{Find } u_S \in S \text{ such that } b(u_S,v) = (f,v), \quad \forall v \in S, \tag{6.20}$$

At first glance one may think that there are multiple solutions to (6.20), since the equation only needs to hold for a v in a subset of H_0^1. However, there is a unique solution to (6.20). Therefore (6.20) defines a solution. We formalize this in a theorem.

Theorem 6.3.1. *For any $f \in L^2(0,L)$, (6.20) has a unique solution $u_S \in S$.*

Proof. The proof for this theorem is analogous to the proof of Theorem 6.2.3, where in the proof we change H_0^1 to S. Note that this is allowed because since S is a subset of a Hilbert space, it is itself a Hilbert space. □

This theorem implies that the approximate problem (6.20) defines an approximate solution u_S. If we choose the subspace S to be finite dimensional, then we can numerically find this approximate solution. How this is done is explained in section 7. It turns out that the approximation defined by problem (6.20) is the best approximation in S, with respect to the *energy norm*, which is defined as

$$\|v\|_E = \sqrt{b(v,v)}. \tag{6.21}$$

To see that (6.21) does indeed define a norm, one can check that $b(v,v)$ is an inner product.

Lemma 6.3.2. *Let u be the solution to (6.6) and u_S be the solution to (6.20). Then*

$$\|u - u_S\|_E = \inf_{v \in S} \|u - v\|_E. \tag{6.22}$$

Proof. First, observe that by subtracting (6.20) from (6.6), we have for any $v \in S$,

$$b(u - u_S, v) = 0. \tag{6.23}$$

This is called the *Galerkin orthogonality*. Additionally, observe the following Schwarz' inequality:

$$b(v, w) \leq \|v\|_E \|w\|_E, \quad \forall v, w \in H_0^1. \tag{6.24}$$

For any $v \in S$, we have

$$\begin{aligned} \|u - u_S\|_E^2 &= b(u - u_S, u - u_S) \\ &= b(u - u_S, u - v) + b(u - u_S, v - u_S) \\ &= b(u - u_S, u - v) \\ &\leq \|u - u_S\|_E \|u - v\|_E. \end{aligned}$$

In this derivation we use the fact that $v - u_S \in S$, in combination with (6.23). If $\|u - u_S\|_E = 0$, then we can divide out $\|u - u_S\|_E$ to find that $\|u - u_S\|_E \leq \|u - v\|_E$ for all $v \in S$. If $\|u - u_S\|_E = 0$, this inequality holds trivially. Therefore

$$\|u - u_S\|_E \leq \inf_{v \in S} \|u - v\|_E. \tag{6.25}$$

Since $u_s \in S$, inequality cannot hold. □

This is an important result. It states that with respect to the energy norm, the solution to (6.20) gives the best approximation to u. This means that we can numerically approximate u by choosing an appropriate subspace $S \subset H_0^1$. We will discuss two choices of subspaces S.

6.4 Lagrangian basis functions

The choice of subspace S in which one tries to approximate the solution to (6.6) informs the approximate solution. Therefore it may pay off to think about the space carefully. First, we consider a fairly straightforward choice.

Let $Y_N = \{y_0, \ldots, y_N\}$ be a partition of $(0, L)$, such that $\mathcal{P} \subset Y_N$. That means that the discontinuities in a are covered by Y_N. We introduce piecewise linear functions with respect to these points, that will serve as basis functions to approximate the solution u. These functions are defined as

$$\phi_i(z) = \begin{cases} \frac{z - y_{i-1}}{y_i - y_{i-1}} & y_{i-1} < z < y_i, \\ \frac{y_{i+1} - z}{y_{i+1} - y_i} & y_i \leq z < y_{i+1}, \\ 0 & \text{otherwise}, \end{cases} \tag{6.26}$$

for $1 \leq i \leq n-1$. Since Y_N covers all discontinuities of a, a is constant on every open interval (y_i, y_{i+i}). The piecewise linear functions introduced in Equation (6.26) serve as a basis for the subspace in which we can approximate u. Formally,

$$S_N(Y_N) = \left\{ \sum_{j=1}^{n-1} c_j \phi_j : c_j \in \mathbb{R} \right\}. \tag{6.27}$$

Equivalently,

$$S_N(Y_N) = \mathbb{P}(Y_N) \cap H_0^1. \tag{6.28}$$

where $\mathbb{P}(Y_N)$ is the space of piecewise linear functions, with respect to the partition Y_N.

6.5 Micro-macro decomposition

In the previous section we described a general finite elements method using Lagrange basis functions. In this section we look at a different choice of basis functions in order to approximate the function u from (6.6). This method uses the structure of the function a as described in section 6.1 to its advantage. The method uses macro functions which are used to approximate the global behaviour of u and uses micro functions to further approximate local behaviour. We first describe the macro functions and then move on to the micro functions.

6.5.1 Macro functions

The macro functions $\phi_i \in H_0^1$ are defined in a piece-wise manner by the following problem:

$$\begin{cases} \int_{C_j} a\phi_i'\psi' \, dz = 0, \quad \forall \psi \in H_0^1(z_{j-1}, z_j), \quad \forall j \in \{1, \dots, n\}, \\ \phi_i(z_j) = \delta_{ij}, \end{cases} \tag{6.29}$$

where δ_{ij} is the Kronecker delta. This problem is easily solved. Let

$$A_i = \left(\int_{z_{i-1}}^{z_i} \frac{1}{a(t)} \, dt \right)^{-1} \tag{6.30}$$

$$\alpha_i(z) = A_i \int_{z_{i-1}}^{z} \frac{1}{a(t)} \, dt, \quad \text{for } z \in (z_{i-1}, z_i), \tag{6.31}$$

$$\beta_i(z) = A_{i+1} \int_{z}^{z_{i+1}} \frac{1}{a(t)} \, dt, \quad \text{for } z \in (z_i, z_{i+1}). \tag{6.32}$$

Notice that $\alpha_i \in H^1(z_{i-1}, z_i)$ and $\beta_i \in H^1(z_i, z_{i+1})$. Furthermore, the functions β_i satisfy

$$\begin{cases} -(a\beta_i)' = 0 \quad \text{in } (z_i, z_{i+1}), \\ \beta_i(z_i) = 1, \quad \beta(z_{i+1}) = 0. \end{cases} \tag{6.33}$$

and α_i satisfy

$$\begin{cases} -(a\alpha_i)' = 0 \quad \text{in } (z_{i-1}, z_i), \\ \alpha_i(z_{i-1}) = 0, \quad \alpha(z_i) = 1. \end{cases} \tag{6.34}$$

Then it is easy to see that

$$\phi_i(z) = \begin{cases} \alpha_i, & z_{i-1} < z \leq z_i, \\ \beta_i, & z_i < z < z_{i+1}, \\ 0, & \text{otherwise}, \end{cases} \tag{6.35}$$

satisfies (6.29).

6.5.2 Micro functions

For local enrichment, we introduce n_{micro} micro functions on the cells. Each micro function has support only on a single cell. We define the microfunctions as solutions to the eigenproblem

$$\begin{cases} -(a(x){m_j^i}'(z))' = \lambda_j^i m_j^i(z), \quad m_j^i(z_{i-1}) = m_j^i(z_i) = 0, & \text{in } \bar{C}_i, \\ 0, & \text{otherwise.} \end{cases} \tag{6.36}$$

These are essentially eigenfunctions of a Sturm-Liouville problem with homogeneous boundary conditions. This problem has a discrete spectrum. Furthermore, these microfunctions satisfy

$$\int_{C_i} a{m_j^i}'\psi' \, dz = \lambda_j^i \int_{C_i} m_j^i \psi \, dz \quad \forall \psi \in H_0^1(C_i). \tag{6.37}$$

This implies the weak form

$$b(m_j^i, v) = (m_j^i, v)\lambda_j^i, \quad \forall v \in H_0^1. \tag{6.38}$$

We normalize the micro functions by setting

$$(m_j^i, m_j^i) = 1. \tag{6.39}$$

Furthermore, we order the eigenvalues such that $\lambda_j^i \leq \lambda_{j+1}^i$, for all $i \in \{1, \dots, n\}$, $j \in \mathbb{N}$. Since the left hand side of (6.36) is a Hermitian operator working on m_j^i, it follows that all functions m_j^i are eigenfunctions of a Hermitian operator. Therefore the eigenfunctions are all orthogonal and dense in H_0^1.

Remark 6.5.1. Computation of the eigenfunctions and corresponding eigenvalues can be done via the finite elements method as described in Section 6.4. Moreover, since there are only p different cell types $\hat{C}_k$, for $k \in \{1, \dots, p\}$, it is sufficient to compute the eigensystem for

$$-(a_k(z)\hat{m}_j^{k\prime}(z))' = \hat{\lambda}_j^k \hat{m}_j^k(z), \quad \hat{m}_j^k(0) = \hat{m}_j^k(\hat{c}_k) = 0, \quad \text{in } \hat{C}_k, \tag{6.40}$$

for $k \in \{1, \dots, p\}$. The full eigensystem $\{(m_j^i, \lambda_j^i)\}_j$ can be obtained via a simple translation $\hat{z} \to \hat{z} + z_{i-1}$ for $\hat{z} \in (0, \hat{c}_k)$ to the corresponding cell C_i.

Remark 6.5.2. Notice that $m_j^i \in H_0^1(C_k)$, for all $i, k \in \{1, n\}$, $j \in \mathbb{N}$. Therefore, by (6.29), we have the orthogonality relation

$$b(\phi_k, m_j^i) = 0, \tag{6.41}$$

for all $k \in \{1, \dots, n-1\}$.

6.5.3 Combining

Now that we have defined basis functions, we can define the space in which we search for an approximation. Since we need a finite dimensional space in order to find a numerical solution, we use the first m micro functions for each cell. We define the space

$$S_m^{\text{mm}} = \left\{ v_h = \sum_{i=1}^{n-1} c_i \varphi_i + \sum_{i=1}^{n} \sum_{j=1}^{m} d_{ij} m_j^i : c_i, d_{ij} \in \mathbb{R} \right\}, \tag{6.42}$$

where mm refers to the micro-macro decomposition.

6.6 Convergence

6.6.1 Lagrange basis functions

We have introduced different choices of subspaces H_0^1, in which we find an approximate solution to problem (6.6). In this subsection we compare the convergence rates of these choices. More precisely, we look at how fast the approximate solution converges to the exact solution if we increase the dimensionality of the subspace. First we consider the convergence of the standard finite element method with Lagrange basis functions.

Lemma 6.6.1. *Let $\mathcal{T}_h := \{y_i : i \in \{0, \dots, N\}\}$ be a partition of $(0, L)$ that resolves $\mathcal{P}$. Let $S_N = \mathbb{P}_1(\mathcal{T}_h) \cap H_0^1$ be the finite element space of piecewise linear functions w.r.t. $\mathcal{T}_h$, as defined in Section 6.4. Furthermore, let $\mathcal{T}_h$ be quasi-uniform, i.e. there exists a constant c_h, such that*

$$\min_{i \in \{0, \dots, N-1\}} y_{i+1} - y_i \geq c_h \max_{i \in \{0, \dots, N-1\}} y_{i+1} - y_i, \tag{6.43}$$

Furthermore, let

$$b(u_N, v) = (f, v), \quad \forall v \in S_N, \tag{6.44}$$

for some $u_N \in S_N$ and let u be the solution to (6.6). Then for some finite $K_1, K_2 \in \mathbb{R}$,

(a) $\|u' - u'_N\|_{L^2(0,L)} \leq K_1 N^{-1}$,

(b) $\|u - u_N\|_{L^2(0,L)} \leq K_2 N^{-2}$,

where K_1, K_2 *depend on* $\|f\|_{L^2(0,L)}$.

Proof. First observe the following. For any $v \in H^1(a,b)$, with $v(c) = 0$, for some $c \in (a,b)$, we have

$$\int_a^b v^2 dz \leq \int_a^b \left(\int_c^x v(c) + v'(t)\, dt \right)^2 dz \leq \int_a^b \left(\int_a^b |v'(t)|\, dt \right)^2 dz \leq (b-a) \int_a^b |v'|^2 dz. \tag{6.45}$$

Additionally, for any $v \in L^2(a,b)$, we have

$$\left(\int_a^b v dz \right)^2 \leq \left(\int_a^b 1^2 dz \right) \left(\int_a^b |v|^2 dz \right) = (b-a) \left(\int_a^b |v|^2 dz \right). \tag{6.46}$$

Now, let $\bar{u}_N$ be the piecewise linear interpolant of u. That is, let

$$\bar{u}_N = \sum_{j=1}^{N-1} c_j \phi_j, \tag{6.47}$$

where $c_j = u(x_j)$ and ϕ_j are as defined in (6.35). We will obtain an upper bound for the error in derivative between u and $\bar{u}_N$. First, we split up the error in integrals:

$$\|u' - \bar{u}'_N\|^2_{L^2(0,L)} = \int_0^L (u' - \bar{u}'_N)^2\, dz = \sum_{j=0}^{N-1} \int_{y_j}^{y_{j+1}} (u' - \bar{u}'_N)^2\, dz. \tag{6.48}$$

Let $w := u - \bar{u}_N$. We see that $w(y_i) = 0$, for all $i \in \{1, \ldots, n\}$. Furthermore, since the partition $\mathcal{T}_h$ resolves $\mathcal{P}$, there is some interval (x_j, x_{j+1}) such that $(y_i, y_{i+1}) \subset (x_j, x_{j+1})$. Thus, by Lemma 6.2.4, $u\big|_{(y_i,y_{i+1})} \in H^2(y_i, y_{i+1})$. Additionally, $\phi_i\big|_{(y_i,y_{i+1})} \in \mathbb{P}_1(y_i, y_{i+1}) \subset H^2(y_i, y_{i+1})$. Therefore $w\big|_{(y_i,y_{i+1})} \in H^2(y_i, y_{i+1})$. Now, since $w(y_i) = w(y_{i+1})$, by Rolle's theorem, there exists some $\alpha_i \in (y_i, y_{i+1})$, such that $w'(\alpha_i) = 0$. Therefore, we can apply (6.45) and (6.46) to find

$$\|w'\|^2_{L^2(0,L)} \leq \sum_{i=1}^{N} h_i^2 \int_{y_i}^{y_{i+1}} |w''|^2\, dz = \sum_{i=1}^{N} h_i^2 \int_{y_i}^{y_{i+1}} |u''|^2\, dz. \tag{6.49}$$

On (y_i, y_{i+1}), a is constant. Therefore $-u'' = f/a$ on (y_i, y_{i+1}). Then

$$\sum_{i=1}^{N} h_i^2 \int_{y_i}^{y_{i+1}} |u''|^2\, dz = \sum_{i=1}^{N} h_i^2 \int_{y_i}^{y_{i+1}} \left| \frac{f}{a} \right|^2 dz \leq \sum_{i=1}^{N} \left(\frac{c_h}{N} \right)^2 \int_{y_i}^{y_{i+1}} \left| \frac{f}{a} \right|^2 dz \leq \left(\frac{c_h}{N} \right)^2 C^2 \int_0^L |f|^2\, dz. \tag{6.50}$$

Applying (6.50) to (6.49) yields

$$\|w'\|_{L^2(0,L)} \leq C \left(\frac{c_h}{N} \right) \|f\|_{L^2(0,L)}. \tag{6.51}$$

By Lemma 6.3.2, u_N must approximate u at least as good as $\bar{u}_N$, with respect to the energy norm. Therefore

$$\|u' - u'_N\|_{L^2(0,L)} \leq \sqrt{C} \|u - u_N\|_E \leq \sqrt{C} \|u - \bar{u}_N\|_E \leq C \|w'\|_{L^2(0,L)} \leq \frac{K_1}{N}, \tag{6.52}$$

with $K_1 = C^2 c_h \|f\|_{L^2}$. This proves (a). Now, let χ be the defined as the weak solution to the dual problem

$$-(a\chi')' = u - u_N \quad \text{in } (0,L), \quad \text{with } \chi(0) = \chi(L) = 0. \tag{6.53}$$

That is, let χ be the solution to

$$b(v,\chi) = (u - u_N, v), \quad \forall v \in H_0^1 \tag{6.54}$$

Since $u - u_N \in H_0^1$, it follows that

$$\|u - u_N\|_{L^2}^2 = (u - u_N, u - u_N) = b(u - u_N, \chi) = b(u - u_N, \chi - v), \tag{6.55}$$

for arbitrary $v \in S_N$. The last equality results from Galerkin orthogonality, as in (6.23). Now let $v_h \in S_N$ be the solution to

$$b(v, v_h) = (u - u_N, v), \quad \forall v \in S_N. \tag{6.56}$$

Note that if we take (6.6) and (6.44) and substitute $u \to \chi$, $u_N \to v_h$ and $f \to u - u_N$, then we get exactly (6.54) and (6.56), respectively. Therefore, by the same reasoning to get (6.52), we obtain

$$\|\chi' - v_h'\|_{L^2} \leq \frac{C^2 c_h}{N} \|u - u_N\|_{L^2}. \tag{6.57}$$

Using (6.52) and (6.57) in (6.55) it follows that

$$\begin{aligned} \|u - u_N\|_{L^2}^2 &\leq \|u - u_N\|_E \|\chi - v_h\|_E \\ &\leq \sqrt{C}\|u' - u_N'\|_{L^2} \sqrt{C}\|\chi' - v_h'\|_{L^2} \\ &\leq C\left(K_1 N^{-1}\right)\left(K_1 N^{-1}\|u - u_N\|_{L^2}\right). \end{aligned}$$

Dividing by $\|u - u_N\|_{L^2}$ yields

$$\|u - u_N\|_{L^2} \leq \frac{K_2}{N^2}, \tag{6.58}$$

where $K_2 = K_1^2 C$. This proves (b).

□

6.6.2 Micro-macro decomposition

Now we look at the convergence of the micro-macro decomposition method. Since the number of cells is determined by the problem, the only free variable is the choice of the number of micro functions. We look at the convergence as the number of micro functions increases.

Lemma 6.6.2. *Let S_m^{mm} be the space spanned by the micro functions and macrofunctions, as defined in* (6.42)*. Let u_m be the solution to* (6.20)*, for $S = S_m^{mm}$. Furthermore, let m_j^i be the micro scale functions as defined by* (6.36)*. Moreover, let $\Pi_m : L^2(0,L) \to L^2(0,L)$ be the operator defined by*

$$\Pi_m g = \sum_{i=1}^{n}\sum_{j=1}^{m}\left(\int_0^L g m_j^i \, dz\right) m_j^i. \tag{6.59}$$

Then for some finite $K_1, K_2 \in \mathbb{R}$,

(a) $\|u' - u_m'\|_{L^2} \leq K_1/m \|f - \Pi_m f\|_{L^2(0,L)}$. (first)

(b) $\|u - u_m\|_{L^2} \leq K_2/m^2 \|f - \Pi_m f\|_{L^2(0,L)}$. (duality)

Proof. Let $w := u - \sum_{i=1}^{n-1} u(z_i)\phi_i$, where ϕ_i are as defined in (6.29). We now will approximate w by a truncated expansion of the micro functions.

$$w_m = \sum_{i=1}^{n}\sum_{j=1}^{m} c_{ij} m_j^i, \tag{6.60}$$

where the Fourier coefficients c_{ij} are given by

$$c_{ij} = \int_0^L w m_j^i \, dx = \frac{1}{\lambda_j^i} \int_0^L a w' m_j^{i\prime} \, dz = \frac{1}{\lambda_j^i} \int_0^L a u' m_j^{i\prime} \, dz = \frac{1}{\lambda_j^i} \int_0^L f m_j^i \, dz. \tag{6.61}$$

The second equality holds because m_j^i and ϕ_i are orthogonal. Furthermore, since $m_j^i \in H_0^1$, the third and fourth equality follow from (6.38) and (6.6), respectively. Recall that the micro functions m_j^i have support on only one cell each. On cell C_i, we have that $w = \sum_{j=1}^{\infty} c_{ij} m_j^i$. Therefore, by completeness of $\{m_j^i\}$,

$$\begin{aligned}
\|w' - w_m'\|_{L^2(0,L)}^2 &= \sum_{i=1}^{n} \int_{C_i} (w' - w_m')^2 \, dx = \sum_{i=1}^{n} \int_{C_i} \left(\sum_{j=m+1}^{\infty} c_{ij} m_j^{i\prime} \right)^2 dz \\
&\leq C \sum_{i=1}^{n} \sum_{j,k=m+1}^{\infty} c_{ij} c_{ik} \int_{C_i} a m_j^{i\prime} m_k^{j\prime} \, dz = C \sum_{i=1}^{n} \sum_{j,k=m+1}^{\infty} c_{ij} c_{ik} \lambda_j^i \int_{C_i} m_j^i m_k^i \, dz \\
&= C \sum_{i=1}^{n} \sum_{j=m+1}^{\infty} c_{ij}^2 \lambda_j^i.
\end{aligned}$$

Asymptotic behaviour of the eigenvalues is given by[33, p 415]

$$\lim_{j \to \infty} \frac{\lambda_j^i}{j^2} = \pi^2 \left(\int_{C_i} \sqrt{1/a} \, dz \right)^{-2}. \tag{6.62}$$

Therefore must be a constant $C_\lambda > 0$, such that $j^2/C_\lambda \leq \lambda_j^i \leq C_\lambda j^2$. Then we have, from (6.48)

$$\begin{aligned}
\|w' - w_m'\|_{L^2(0,L)}^2 &= C \sum_{i=1}^{n} \sum_{j=m+1}^{\infty} \frac{1}{\lambda_j^i} (f, m_j^i)^2 \leq C C_\lambda \sum_{i=1}^{n} \sum_{j=m+1}^{\infty} \frac{1}{j^2} (f, m_j^i)^2 \\
&\leq \frac{C C_\lambda}{m^2} \|f - \Pi_m f\|_{L^2(0,L)}^2.
\end{aligned}$$

Now let $v_h = \sum_{i=1}^{n-1} u(z_i)\phi_i + w_m$. Then

$$\|u' - v_h'\|_{L^2(0,L)} \leq \|w' - w_m'\|_{L^2(0,L)} \leq \frac{\sqrt{C C_\lambda}}{m} \|f - \Pi_m f\|_{L^2(0,L)}, \tag{6.63}$$

Notice that $v_h \in S_m^{\text{mm}}$. Therefore, by Lemma 6.3.2 u_m must be a better approximation of u in the sense of the energy norm.
Therefore

$$\|u - u_m\|_E \leq \|u - v_h\|_E \leq \sqrt{C} \|u' - v_h'\|_{L^2(0,L)} \leq \frac{C\sqrt{C_\lambda}}{m} \|f - \Pi_m f\|_{L^2(0,L)}. \tag{6.64}$$

Thus, we have proven (a). Now we prove (b). Let

$$-(a\chi')' = u - u_m \quad \text{in } (0, L), \quad \text{with } \chi(0) = \chi(L) = 0. \tag{6.65}$$

That is, let χ be the solution to

$$b(v, \chi) = (u - u_m, v), \quad \forall v \in H_0^1. \tag{6.66}$$

Since $u - u_m \in H_0^1$, it follows that

$$\|u - u_m\|_{L^2}^2 = (u - u_m, u - u_m) = b(u - u_m, \chi) = b(u - u_m, \chi - v), \tag{6.67}$$

for arbitrary $v \in S_m^{\text{mm}}$. The last equality results from Galerkin orthogonality, as in (6.23). Now let $\chi \in S_m^{\text{mm}}$ be the solution to

$$b(v, v_h) = (u - u_m, v), \quad \forall v \in S_m^{\text{mm}}. \tag{6.68}$$

By the same reasoning to get (6.64), we obtain

$$\|\chi' - v_h'\|_{L^2} \leq \frac{\sqrt{CC_\lambda}}{m}\|u - u_m - \Pi_m(u - u_m)\|_{L^2} \leq \frac{\sqrt{CC_\lambda}}{m}\|u - u_m\|_{L^2}. \tag{6.69}$$

Using (6.64) and (6.69) in (6.67) it follows that

$$\begin{aligned}\|u - u_m\|_{L^2}^2 &\leq \|u - u_m\|_E\|\chi - v_h\|_E \\ &\leq \frac{C\sqrt{C_\lambda}}{m}\|f - \Pi_m f\|_{L^2(0,L)}\sqrt{C}\|\chi' - v_h'\|_{L^2} \\ &\leq \frac{C\sqrt{C_\lambda}}{m}\|f - \Pi_m f\|_{L^2(0,L)}\frac{C\sqrt{C_\lambda}}{m}\|u - u_m\|_{L^2}.\end{aligned}$$

Dividing by $\|u - u_m\|_{L^2}$ yields

$$\|u - u_m\|_{L^2} \leq \frac{C^2C_\lambda}{m^2}\|f - \Pi_m f\|_{L^2(0,L)}^2, \tag{6.70}$$

which proves (b).

□

This is an interesting result. Since $\|f - \Pi_m f\|_{L^2(0,L)}$ is nonincreasing with m, we have at least linear convergence in H^1. Similarly, we have at least quadratic convergence in L^2. If f is in $H^1(0, L)$, we get better convergence.

Lemma 6.6.3. *Let $f \in H_0^1(0, L)$. Let Π be the operator as defined in 6.59. Then for some finite $K \in \mathbb{R}$,*

$$\|f - \Pi_m f\|_{L^2(0,L)} \leq K/\sqrt{m}. \tag{6.71}$$

Proof. Recall that

$$\|f - \Pi_m f\|_{L^2(0,L)}^2 = \sum_{j=m+1}^{\infty}(f, m_j^i)^2. \tag{6.72}$$

Since $f \in H_0^1(0, L)$ by assumption, the following integration by parts is allowed, where we use (6.36) to substitute m_j^i:

$$\begin{aligned}(f, m_j^i) &= \int_0^L f m_j^i\, dz = \frac{1}{\lambda_j^i}\int_0^L a m_j^{i\prime} f'\, dz \\ &\leq \frac{\sqrt{C}}{\lambda_j^i}\|m_j^{i\prime}\|_{L^2(0,L)}\|f'\|_{L^2(0,L)}.\end{aligned}$$

Observe by (6.38) that

$$\|m_j^{i\prime}\|_{L^2(0,L)}^2 = (m_j^{i\prime}, m_j^{i\prime}) \leq Cb(m_j^i, m_j^i) = C\lambda_j^i(m_j^i, m_j^i) = C\lambda_j^i. \tag{6.73}$$

It follows that

$$(f, m_j^i) \leq \frac{C}{\sqrt{\lambda_j^i}}\|f'\|_{L^2(0,L)}. \tag{6.74}$$

$\|f'\|_{L^2(0,L)}^2$ is finite, since $f \in H_0^1(0, L)$. Furthermore, from (6.62), we know that there must be a constant $C_\lambda > 0$, such that $j^2/C_\lambda \leq \lambda_j^i \leq C_\lambda j^2$. Hence

$$\|f - \Pi_m f\|_{L^2(0,L)}^2 \leq \sum_{j=m+1}^{\infty}\frac{C^2C_\lambda^2}{j^2}\|f'\|_{L^2(0,L)}^2 \leq \frac{K}{m}, \tag{6.75}$$

for some $K \in \mathbb{R}$ depending on $\|f'\|_{L^2(0,L)}$.

□

7 Implementation

In order to find Ritz-Galerkin approximation in a subspace $S \subset H_0^1$, we have to find the solution to (6.20). Let $\{\varphi_i : i \in \{1, \dots, N\}\}$, with $\varphi_i \in H_0^1$, be a basis of S. Furthermore, let u_S be the solution to (6.20). This solution must be of the form

$$u_S = \sum_{j=1}^{N} c_j \varphi_j, \tag{7.1}$$

for real constants c_j. Using this form of u_S and setting $v = \varphi_k$ in (6.20) yields

$$\text{Find } \{c_j : j \in \{1, \dots, N\}\} \text{ such that } \sum_{j=1}^{N} c_j b(\varphi_j, \varphi_k) = (f, \varphi_k). \tag{7.2}$$

This is equivalent to solving the matrix equation

$$Ac = g, \tag{7.3}$$

for c, where $A \in \mathbb{R}^{N \times N}$, $c, g \in \mathbb{R}^N$ and

$$A_{jk} = b(\varphi_j, \varphi_k), \tag{7.4}$$
$$g_k = (f, \varphi_k). \tag{7.5}$$

Note that this holds, since $A_{jk} = A_{kj}$. Since (7.3) is equivalent to (6.20), Theorem 6.2.3 ensures that (7.3) has a unique solution.
Depending on the choice of basis functions, the matrix A may be dense or sparse. In particular, if there are many basis functions which do not have overlapping support, then A will be sparse. For both subspaces that were discussed in the previous chapter, i.e. the subspace spanned by the Lagrangian basis functions, and the subspace spanned by the micro-macro decomposition, there are few basis functions with overlapping support. From this, it is immediately clear that A is a sparse matrix. We will show that for the method using Lagrangian basis functions, A will be a tridiagonal matrix. For the micro-macro decomposition, A will consist of a tridiagonal and a diagonal block.

7.1 Lagrangian basis functions

Let $Y_N = \{y_0, \dots, y_N\}$ be a partition of Ω, such that $\mathcal{P} \subset Y_N$. Let ϕ_i for $i \in \{1, \dots, N\}$ be the Lagrangian basis functions as defined in (6.26) on the basis of Y_N. By construction, ϕ_i only has overlapping support with ϕ_{i-1} and ϕ_{i+1}. Furthermore, since Y_N covers all discontinuities, a is constant on (y_i, y_{i+1}). We define $a_{i+1/2} := a((x_i + x_{i+1})/2)$. Then

$$A_{ij} = \begin{cases} \frac{a_{i-1/2}}{3(x_i - x_{i-1})} + \frac{a_{i+1/2}}{3(x_{i+1} - x_i)} & \text{if } i = j, \\ \frac{a_{i+1/2}}{6(x_{i+1} - x_i)} & \text{if } i = j - 1, \\ \frac{a_{i-1/2}}{6(x_i - x_{i-1})} & \text{if } i = j + 1, \\ 0 & \text{otherwise.} \end{cases} \tag{7.6}$$

7.2 Microfunctions

As stated in Remark 6.5.1, we can compute the microfunctions using the finite elements method with Lagrange basis functions. Looking on a single cell, we have to solve the following eigensystems.

$$-(a_i(z)\hat{m}_j^{i\prime}(z))' = \hat{\lambda}_j^k \hat{m}_j^i(z), \quad \hat{m}_j^i(0) = \hat{m}_j^i(\hat{c}_i) = 0, \quad \text{in } (0, \hat{c}_i), \tag{7.7}$$

for $i \in \{1, \dots, p\}$. This implies the following weak formulation

$$b(\hat{m}_j^i, v) = \hat{\lambda}_j^i(\hat{m}_j^i, v), \quad \forall v \in H_0^1. \tag{7.8}$$

Now let $Y^i = \{y_k\}_{k\in\{0,\dots,n_i\}}$ be some partition of $(0, \hat{c}_i)$. Then we find approximations to $\hat{m}^i_j$ in the space $S_{n_i}(Y^i) = \mathbb{P}_1(Y^i) \cap H^1_0$. Let ϕ_i be the the piecewise linear functions, defined with respect to this partition, let $\phi^i_k \in \mathbb{P}_1(Y^i)$, with $\phi^i_k(y_j) = \delta_{ij}$. We approximate $\hat{m}^i_j$ by

$$w^i_j = \sum_{k=1}^{n_i-1} \alpha^i_{kj}\phi^i_k. \tag{7.9}$$

By the Galerkin approximation, (7.8) leads to

$$\sum_{k=1}^{n_i-1} \alpha^i_{kj} b(\phi^i_k, \phi_l) = \lambda^i_j \sum_{k=1}^{n_i-1} \alpha^i_{kj}(\phi^i_k, \phi_l), \quad \forall l \in \{1, \dots, n_i\}. \tag{7.10}$$

We write this in matrix representation:

$$(A^i)\alpha^i = (M^i)^\top \alpha^i \Lambda^i, \tag{7.11}$$

where

$$(A^i)_{jk} = b(\phi^i_j, \phi^i_k), \tag{7.12}$$
$$(M^i)_{jk} = (\phi^i_j, \phi^i_k), \tag{7.13}$$
$$(\alpha^i)_{jk} = \alpha^i_{jk}, \tag{7.14}$$
$$(\Lambda^i)_{jk} = \lambda^i_j \delta_{jk}. \tag{7.15}$$

Since A^i and M^i are symmetric, we can rewrite (7.11) as a generalized eigenvalue problem:

$$A^i\alpha^i = M^i\alpha^i\Lambda^i. \tag{7.16}$$

7.3 Micro-macro decomposition

Let ϕ_i, for $i \in \{1, \dots, n-1\}$, be the macro functions as defined in subsection 6.5.1. Furthermore, let m_{ij}, for $i \in \{1, \dots, n\}$ and $j \in \{1, \dots, m\}$, be the micro functions as defined in subsection 6.5.2. These functions form the basis of the space S_m. We can order the basis functions as follows

$$\begin{cases} \varphi_i = \phi_i & \text{for } i \in \{1, \dots, n-1\} \\ \varphi_{n-1+i(m-1)+j} = m_{ij}, & \text{for } i \in \{1, \dots, n\}, j \in \{1, \dots, m\}. \end{cases} \tag{7.17}$$

First notice that ϕ_i only have overlapping support with ϕ_{i-1} and ϕ_{i+1}. Therefore $b(\phi_i, \phi_j) = 0$ if $|i - j| > 0$. Additionally, $b(\phi_i, m_{jk}) = 0$, for all i, j, k, due to (6.29). The matrix A, as defined in (7.4), will consist of an $(n-1) \times (n-1)$ tridiagonal block, and an $nm \times nm$ diagonal block. The $(n-1) \times (n-1)$ tridiagonal block corresponds to the macro functions ϕ_i, while the $nm \times nm$ diagonal block corresponds to the micro functions m_{ij}. Knowing this structure of the A means that only the values for these nonzero entries have to be computed.
Recall also that the micro functions m_{ij} and m_{kj} are just a translation of each other, if cells C_i and C_k are of the same cell type. In that case, $b(m_{ij}, m_{ij}) = b(m_{kj}, m_{kj})$. Therefore it is sufficient to calculate $b(\hat{m}_{kj}, \hat{m}_{kj})$ for $j \in \{1, \dots, m\}$ and $p \in \{1, \dots, p\}$. Then $b(m_{ij}, m_{ij}) = b(\hat{m}_{T(i)j}, \hat{m}_{T(i)j})$, where T is the function as defined in section 6.1.

8 Results

In this chapter we will look at the numerical implementations of both the standard finite element method with Lagrangian basis functions and the micro-macro decomposition method. We will look at the convergence of these methods and compare this with the theoretical convergence. Furthermore, we will compare the two methods when using similar degrees of freedom.

8.1 Standard finite element method

We prepared a simple problem for which we can easily find the exact solution. We solve (6.5) for the interval $(0, 1)$, with

$$a(z) = \begin{cases} 1 & \text{if } z \leq \frac{1}{2}, \\ 2 & \text{if } z > \frac{1}{2}, \end{cases} \tag{8.1}$$

with $f(z) = 1$. The exact solution is given by

$$u(z) = \begin{cases} \frac{z\left(\frac{5}{6} - z\right)}{2} & \text{if } z \leq \frac{1}{2}, \\ \frac{\left(\frac{1}{6} + z\right)(1 - z)}{4} & \text{if } z > \frac{1}{2}. \end{cases} \tag{8.2}$$

Figure 8.1a shows this exact solution and three approximations of this solution, which are obtained by the finite element method using Lagrange basis functions. Figure 8.1b shows the convergence of the finite element method using Lagrange basis functions. This figure clearly shows that asymptotically, the L^2 error of the approximations go like N^{-2}. Additionally, the error between the derivative of the approximation and the derivative of the exact solution goes like N^{-2}. This is exactly what we expected, by Lemma 6.6.1.

8.2 Convergence of micro functions

We prepared a test case with

$$a(z) = \begin{cases} 1 & \text{if } z \leq \frac{1}{2}, \\ 5 & \text{if } z > \frac{1}{2}. \end{cases} \tag{8.3}$$

We approximate the solution to (6.36) for the smallest and fifth smallest eigenvalue respectively, using the finite element method with Lagrange basis functions. Figure 8.2a shows approximations of this first micro function, for different degrees of freedom. Figure 8.2b shows the convergence to this micro function, using the finite elements with Lagrange basis functions. We see that the finite element method with Lagrange basis functions has the same rate of convergence for (6.5) and (6.36). Similarly, Figure 8.2c shows approximations of this first micro function, for different degrees of freedom and Figure 8.2d shows the convergence to this micro function, using the finite elements with Lagrange basis functions. Figures 8.2a and 8.2c already show that to approximate the fifth microfunction, we need more degrees of freedom than for the first microfunction. This can also be seen in Figures 8.2b and 8.2d.

8.3 Micro-macro decomposition

We prepared a test scenario on which to test the micro-macro decomposition method. We prepared an array of cells of two distinct types. Associated to these cells are the diffusion coefficient functions

$$a_1(z) = \begin{cases} 1 & \text{if } 0 \leq z < \frac{1}{3}, \\ 2 & \text{if } \frac{1}{3} \leq z < 0.45, \\ 3 & \text{if } 0.45 \leq z < 1, \end{cases} \tag{8.4}$$

$$a_2(z) = \begin{cases} 10 & \text{if } 0 \leq z < 0.3, \\ 0.3 & \text{if } 0.3 \leq z < 0.5. \end{cases} \tag{8.5}$$

The cells are arranged in the following order

12112121121.

Furthermore, we set $f(z) = 1$, for $z \in (0, L)$. We approximated the solution to (6.5) using the micro-macro decomposition finite element method. We computed the microfunctions using the finite element method with Lagrange basis functions on a grid with spacing of at most 0.001. In order to consider the convergence of the micro-macro decomposition method, we need a reference solution. We computed a reference solution using the finite element method with Lagrange basis functions, using a grid with at most a 5×10^{-5} spacing, which includes all discontinuities in a. Figure 8.3b shows the error between the micro-macro decomposition method and the reference solution for an increasing number of microfunctions. This result shows a convergence rate of 2.5 in the L^2 error and a rate of 1.5 in the H^1 error. However, around 500 degrees of freedom, the error stops decreasing. This can probably be explained by the grid resolution which is used for computation of the micro functions. As we saw in section 8.2, for micro functions with a higher corresponding eigenvalue, a finer grid is needed to get a good approximation of the micro functions. It seems that adding more micro functions is therefore not effective beyond a certain point, depending on the resolution of the grid on which the micro functions have been computed.
This means that we need a fine resolution on which to compute the micro functions, which increases computational costs. Increasing the resolution for the micro functions means that we need more computations have to be done to calculate (f, m_{ij}). Since f in principal does not need to have the same quasiperiodicity as a, these calculations have to be done for all microfunctions m_{ij}. However, if this micro-macro decomposition finite element method is applied to problem (5.12), there is no such source term f. This means that in this case, increasing the resolution of the grid on which the microfunctions are computed, only increases the computation time linearly with the number of different unique types of cells that exist in the quasicrystal. On the other hand, when adding more cells to the quasicrystal, it does not matter for computations what the resolution of the micro grid is. This means that when we apply the method to (5.12), having a very fine grid for the micro functions will not pose a problem.

8.4 Conclusion

In order to study the photonic properties of a colloidal quasicrystal, we proposed a finite elements method that is adapted to the structure of a one dimensional colloidal quasicrystal. We applied this method to a simplified problem, inspired Maxwell's equations and found better convergence than for a standard finite elements method with Lagrange basis functions. Furthermore, we found that we need fewer degrees of freedom in order to get a good approximation. We do however need many degrees of freedom for a good approximation of the microfunctions. We are assuming that there only p unique tiling cells, with $p \ll n$, where n is the total number of tiling cells in the quasicrystal. The microfunctions only have to be computed p times, which makes the computation of the microfunctions negligible as n grows large. We therefore have a method that solves the simplified equation much faster than the finite elements method using Lagrange basis functions.

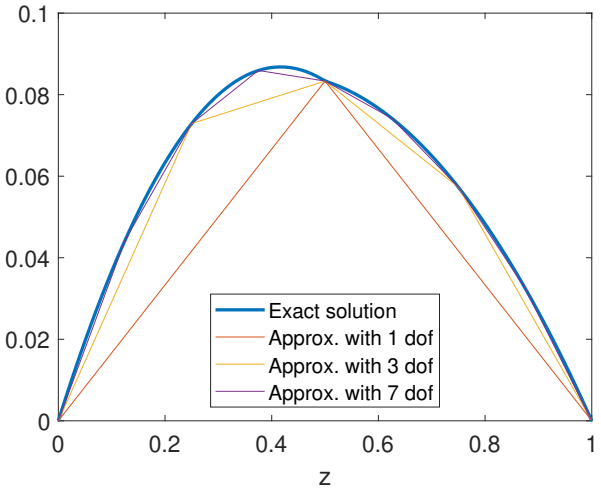

(a) Exact solution and approximations using the finite element method with Lagrange basis functions, with increasing degrees of freedom.

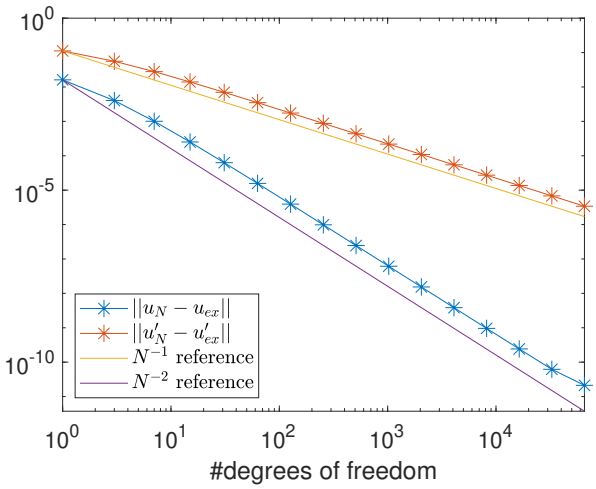

(b) Errors of approximations and their derivatives, for increasing degrees of freedom. Here, u_N are the approximations, while u_{ex} is the exact solution.

Figure 8.1: Approximation and convergence of the finite element method using Lagrange basis functions.

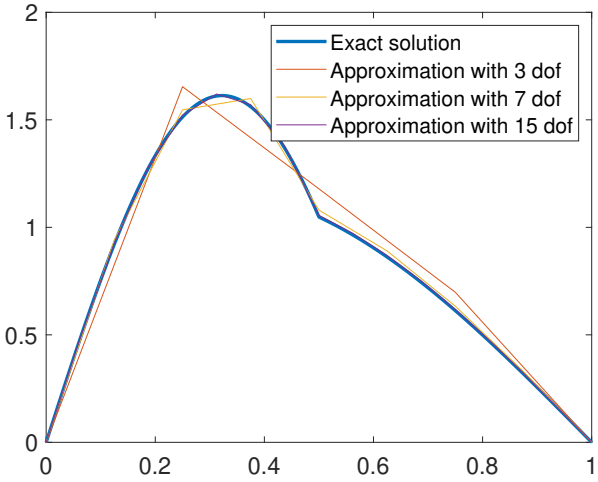

(a) Exact micro function and approximations using the finite element method with Lagrange basis functions, with increasing degrees of freedom.

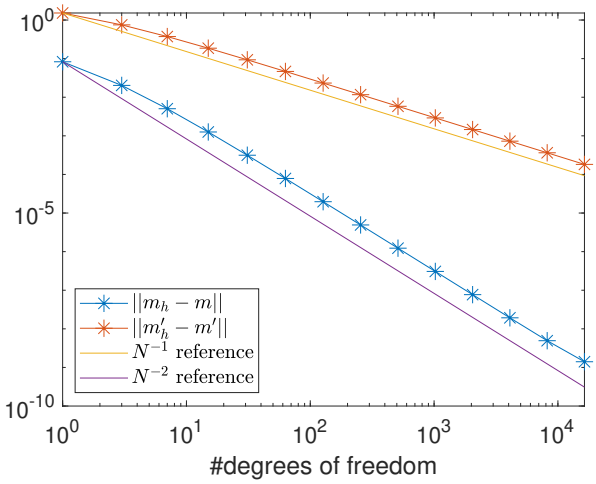

(b) Errors of approximations and their derivatives, for increasing degrees of freedom. Here, m is the exact micro functions, while m_h are the approximations.

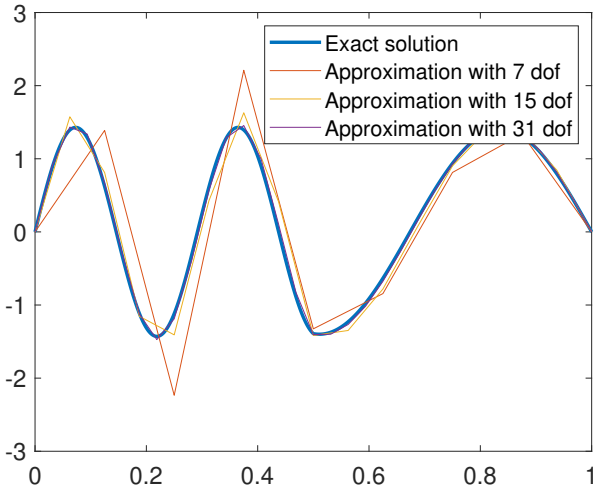

(c) Exact micro function with fifth smallest eigenvalue and its approximations using the finite element method with Lagrange basis functions, with increasing degrees of freedom.

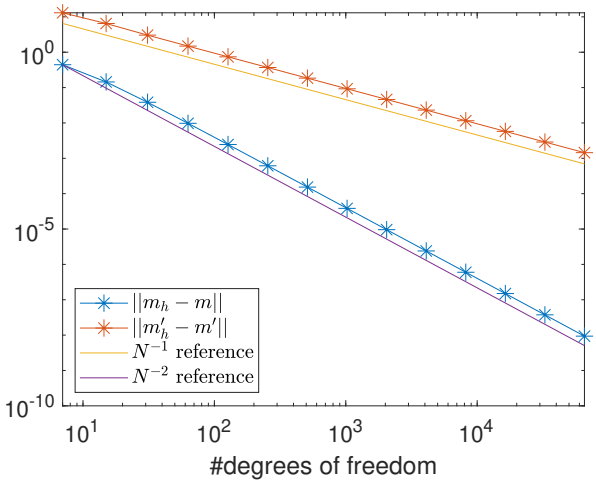

(d) Errors of approximations of the microfunction with fifth smallest eigenvalue and their derivatives, for increasing degrees of freedom. Here, m is the exact micro functions, while m_h are the approximations.

Figure 8.2: Approximations of and convergence to the micro function with first and fifth smallest eigenvalue, respectively, obtained with the finite element method using Lagrange basis functions.

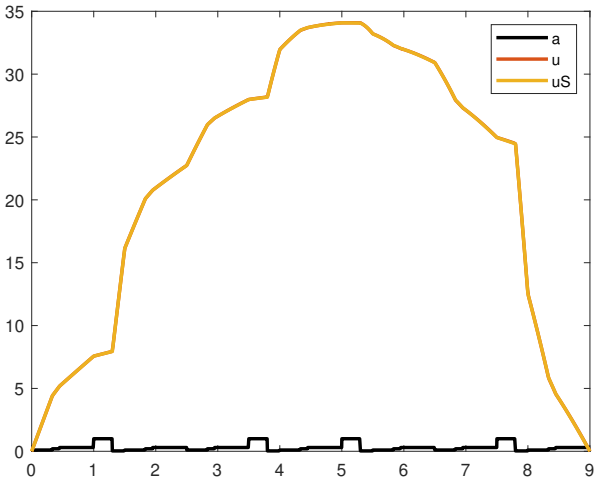

(a) Exact micro function and approximations using the finite element method with Lagrange basis functions, with increasing degrees of freedom.

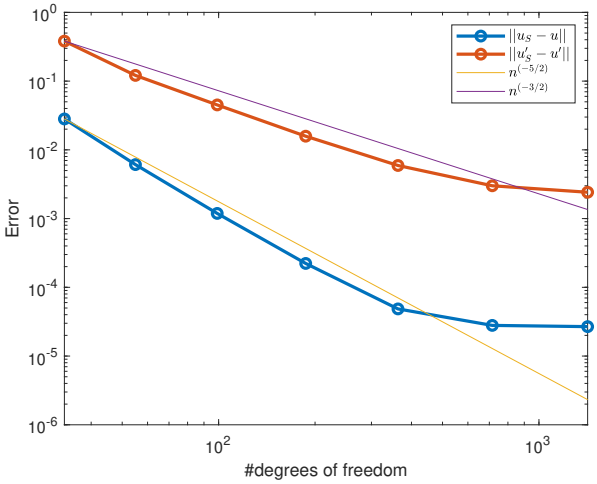

(b) Errors of approximations and their derivatives, for increasing degrees of freedom. Here, m is the exact micro functions, while m_h are the approximations.

PART III

CONCLUSION AND OUTLOOK

Colloidal quasicrystals are considered to be interesting photonic materials, with a potential for exhibiting a full photonic bandgap in the visible spectrum for the right choice of materials. In order to study this potential bandgap, there is a need study both the structure of such quasicrystals as well as predicting their photonic properties, using numerical calculations. In this thesis we have made first steps towards characterizing the structure of a two dimensional self-assembled colloidal quasicrystal consisting of core-corona particles and started to address the problem of predicting the photonic properties of such a quasicrystal.

Specifically, in Part I of this thesis, we studied the self-assembly of a two dimensional system of colloids that was known to form a quasicrystal. We found that the self-assembled structure always contained a large number of defects. In order to look at these defects in detail, we developed an algorithm that was able to identify defects that were associated with vacancies. However, this algorithm still struggled somewhat with identifying the location of defects associated with interstitials, due to their stronger distortion of the quasicrystalline lattice. Furthermore, we used the developed algorithm in order to study the diffusion of defects associated with vacancies. We calculated the diffusion coefficient for such defects for different reduced temperatures T^* and packing fractions η. We found that for low packing fraction and high temperature, the diffusion coefficient was only slightly smaller than the diffusion coefficient of a free colloid.

In part II, we made a first step towards developing a finite elements method which can be used to solve Maxwell's equations on a quasicrystal, allowing us to study the photonic properties and to determine if a band gap exists. We introduced a finite elements method, with micro and macro basis functions. We used this method to solve a simplified problem, inspired by Maxwell's equations on a one dimensional colloidal quasicrystal. We saw that for this problem, our method had better convergence than a standard finite elements method using Lagrange basis functions. This is a promising result. Furthermore, we saw that fewer degrees of freedom are needed to solve this simplified problem on this one dimensional quasicrystal and reach the same error. For higher dimensions, this will be even more true.

Clearly, the next step in exploring the photonic properties of colloidal quasicrystals is to extend the finite elements method to the two dimensional quasicrystal. In the extension to two dimensions, we can use the structural algorithm from Part I to inform the finite elements method, which is used for these calculations. The tiling cells that we would use in two dimensions can be deduced from the lattice, which is constructed by the structural algorithm from Part I.

References

[1] R. B. Perry, "Principles of colloid and surface chemistry, second edition (hiemenz, p. c.)," *Journal of Chemical Education*, vol. 64, no. 12, p. A328, 1987.

[2] D. J. Shaw, "1 - the colloidal state," in *Introduction to Colloid and Surface Chemistry (Fourth Edition)* (D. J. Shaw, ed.), pp. 1–20, Oxford: Butterworth-Heinemann, fourth edition ed., 1992.

[3] R. Mazo, *Brownian Motion: Fluctuations, Dynamics, and Applications*, vol. 112. Oxford University Press, 01 2002.

[4] A. Einstein, "Über die von der molekularkinetischen theorie der wärme geforderte bewegung von in ruhenden flüssigkeiten suspendierten teilchen," *Annalen der Physik*, 1905.

[5] V. Prasad, D. Semwogerere, and E. R. Weeks, "Confocal microscopy of colloids," *Journal of Physics: Condensed Matter*, vol. 19, p. 113102, feb 2007.

[6] Y. Jin and H. A. Makse, "A first-order phase transition defines the random close packing of hard spheres," *Physica A: Statistical Mechanics and its Applications*, vol. 389, no. 23, pp. 5362–5379, 2010.

[7] H. Pattabhiraman, *Quasi-periodic and periodic photonic crystals: A simulation study of their self-assembly, stability and photonic properties*. PhD thesis, Utrecht University, 7 2017.

[8] S. Glotzer, "Quasicrystals: the thrill of the chase," *Nature*, 1 2019.

[9] D. Shechtman, I. Blech, D. Gratias, and J. W. Cahn, "Metallic phase with long-range orientational order and no translational symmetry," *Phys. Rev. Lett.*, vol. 53, pp. 1951–1953, Nov 1984.

[10] A. Jha, "Dan shechtman: 'linus pauling said i was talking nonsense'," *The Guardian*, 1 2013.

[11] K. Chang, "Israeli scientist wins nobel prize for chemistry," *The New York Times*, 10 2011.

[12] N. Rivier, "Non-stick quasicrystalline coatings," *Journal of Non-Crystalline Solids*, vol. 153-154, pp. 458–462, 1993. Proceddings of the Fourth International Conference on Quasicrystals.

[13] M. Kalman, "The quasicrystal laureate," *MIT Technology Review*, 11 2011.

[14] K. Sakoda, *Optical Properties of Photonic Crystals*. Springer Series in Optical Sciences, Springer Berlin Heidelberg, 2004.

[15] L. Biró, K. Kertész, Z. Vértesy, G. Márk, Z. Bálint, V. Lousse, and J.-P. Vigneron, "Living photonic crystals: Butterfly scales — nanostructure and optical properties," *Materials Science and Engineering: C*, vol. 27, no. 5, pp. 941–946, 2007. EMRS 2006 Symposium A: Current Trends in Nanoscience - from Materials to Applications.

[16] F. Meseguer, "Colloidal crystals as photonic crystals," *Colloids and Surfaces A: Physicochemical and Engineering Aspects*, vol. 270-271, pp. 1–7, 2005. Liquids and MesoScience.

[17] Y. An, Z. Gao, and Z. Ouyang, "Surface wave photonic quasicrystal," *Applied Physics Letters*, 4 2020.

[18] Z. V. Vardeny, A. Nahata, and A. Agrawal, "Optics of photonic quasicrystals," *Nature Photonics*, vol. 7, pp. 177–187, Mar 2013.

[19] M. M. Harding, D. C. Hodgkin, A. F. Kennedy, A. O'Connor, and P. Weitzmann, "The crystal structure of insulin: Ii. an investigation of rhombohedral zinc insulin crystals and a report of other crystalline forms," *Journal of Molecular Biology*, vol. 16, no. 1, pp. 212–IN30, 1966.

[20] P. J. Steinhardt, H.-C. Jeong, K. Saitoh, M. Tanaka, E. Abe, and A. P. Tsai, "Experimental verification of the quasi-unit-cell model of quasicrystal structure," *Nature*, vol. 396, pp. 55–57, Nov 1998.

[21] T. Dotera, T. Oshiro, and P. Ziherl, "Mosaic two-lengthscale quasicrystals," *Nature*, vol. 506, pp. 208–211, Feb 2014.

[22] M. Zu, P. Tan, and N. Xu, "Forming quasicrystals by monodisperse soft core particles," *Nature Communications*, vol. 8, p. 2089, Dec 2017.

[23] Q. Gong and X. Hu, *Photonic Crystals: Principles and Applications*. Pan Stanford Publishing, 2014.

[24] R. Wehrspohn, A. Rhein, and T. Geppert, *Photonic Crystals: Principles and Applications*, p. 2. Elsevier, 12 2006.

[25] S. S. M. Cheng, L.-M. Li, C. T. Chan, and Z. Q. Zhang, "Defect and transmission properties of two-dimensional quasiperiodic photonic band-gap systems," *Phys. Rev. B*, vol. 59, pp. 4091–4099, Feb 1999.

[26] N. Metropolis, A. W. Rosenbluth, M. N. Rosenbluth, A. H. Teller, and E. Teller, "Equation of state calculations by fast computing machines," *The Journal of Chemical Physics*, vol. 21, no. 6, pp. 1087–1092, 1953.

[27] M. Oxborrow and C. Henley, "Oxborrow,m. , henley,c. l. random square-triangle tilings: A model for twelvefold-symmetric quasicrystals. phys. rev. b 48, 6966-6998," *Physical review. B, Condensed matter*, vol. 48, pp. 6966–6998, 10 1993.

[28] E. Tondl, M. Ramsay, P. Harrowell, and A. Widmer-Cooper, "Defect-mediated relaxation in the random tiling phase of a binary mixture: Birth, death and mobility of an atomic zipper," *The Journal of chemical physics*, vol. 140, p. 104503, 03 2014.

[29] M. Oxborrow and C. L. Henley, "Random square-triangle tilings: A model for twelvefold-symmetric quasicrystals," *Phys. Rev. B*, vol. 48, pp. 6966–6998, Sep 1993.

[30] I. Babuška, "Error-bounds for finite element method.," *Numerische Mathematik*, vol. 16, pp. 322–333, 1970/71.

[31] S. Brenner and R. Scott, *The Mathematical Theory of Finite Element Methods*. Texts in Applied Mathematics, Springer New York, 2007.

[32] L. Evans, *Partial Differential Equations*. Graduate studies in mathematics, American Mathematical Society, 2010.

[33] R. Courant and D. Hilbert, *Application of the Calculus of Variations to Eigenvalue Problems*, ch. 6, pp. 397–465. John Wiley & Sons, Ltd, 1989.

Acknowledgements

First and foremost, I would like to thank my supervisors Laura Filion from the Debye Institute of Nanomaterial Sciences and Matthias Schlottbom from the University of Twente, for their intensive supervison. They have guided me through the process of writing this thesis and have been very generous with their time. I am also grateful to Joost de Graaf and Rob Bisseling for making this project possible.
Additionally, I would like to express my gratitude to Frank Smallenburg, who has sent me the code which produces a quasicrystal without any defects. He also sent me some notes on the process of uplifting a quasicrystal.
Furthermore, I would like to thank all the people from the Virtual Soft Condensed Matter group, for the weekly meetings and interesting discussions. It has been very nice to see all the projects progress over the year. Special thanks to Marjolein de Jager, for helping me with my struggle against the cluster, allowing me to perform the necessary simulations.
Last but not least, I would like to thank my roommates, for supplying me with the necessary amounts of coffee during this period of working from home.